Article

Open Access | Vita Microbiology

Hadal high pressure stimulates microbial chitin decomposition in the deepest ocean

Xianhong Zeng[1#], Hengjun Zhu[1,2#], Taoliang Zhang[2#], Yifan Li[4], Wentao Ye[1,2], Aijun Jiang[1,2], Ziheng Wu[1], Shanshan Huang[1,2], Runyao Xiong[1,2], Suen Kit Wu[1], Jing Wang[3], Yangyi Lu[4], Xiang Xiao[*1,2,3], Weishu Zhao[*1,2,3]

Chitin is the ocean's most abundant biopolymer, yet how microbial communities decompose it under the extreme pressure of the hadal zone—Earth's deepest ocean region (> 6 km water depth)—remains unknown. Here we show that hadal high pressure (HHP; > 60 MPa) markedly accelerates the decomposition of highly crystalline α-chitin, with an HHP-favored oxidative route playing a critical role in this acceleration, as supported by pressure-gradient cultivations, chitin characterization, and multi-omic analysis. We further identify Meer1P and Meer2P, to our knowledge, the first AA10-family lytic polysaccharide monooxygenases (LPMOs) characterized from hadal microbiomes, as key enzymes involved in chitin oxidation under HHP. Both enzymes show substantially enhanced chitin-oxidizing activity upon H_2O_2 supply under hadal pressure, providing a key mechanism by which HHP-induced H_2O_2 production accelerates LPMO-mediated chitin oxidation in the hadal biosphere. AA10 LPMOs were also preferentially enriched in hadal environments across 1,098 marine metagenomes (0–11 km water depth). These findings provide new insights into how pressure shapes biopolymer decomposition and organic matter transformation, with H_2O_2-driven LPMO activity contributing to these processes in the deepest ocean.

https://doi.org/10.2738/vita.microbiology.2026.10.0002

INTRODUCTION

The hadal zone (> 6 km water depth) represents the deepest region of the ocean and one of the harshest ecosystems on Earth[1,2], characterized by extreme hydrostatic pressure (HHP; > 60 MPa), near-freezing temperatures, and relative nutrient scarcity[3]. Despite these extreme conditions, *in situ* geochemical measurements have demonstrated that hadal sediments exhibit higher microbial respiration rates than shallower abyssal plains[4–7], suggesting that microbial metabolism is not simply suppressed by HHP. Recent metagenomic surveys have further revealed extraordinary microbial novelty in hadal environments[2], with evidence that HHP selectively shapes microbial community composition and metabolic preferences[8,9], with potential implications for hadal biogeochemical cycling[10–13]. However, how HHP specifically shapes enzymatic mechanisms and reshapes microbial metabolism in the hadal zone remains poorly understood.

Chitin, a recalcitrant polysaccharide composed of N-acetylglucosamine (GlcNAc) monomers, is the most abundant biopolymer in the marine environment, with annual production reaching billions of tons[14]. It serves as a structural component in organisms such as arthropods and fungi[15], and is primarily produced by copepods and other zooplankton[14], and rapidly recycled in the upper ocean[16]; however, a fraction escapes remineralization and reaches the deep seafloor via sinking marine snow[17]. In the hadal zone, this sinking chitin input is supplemented by substantial *in situ* chitin production from amphipod-dominated macrofaunal communities that thrive in trench ecosystems[18,19]. Among its natural polymorphic forms, α-chitin is the predominant form[20] and, owing to its antiparallel chain arrangement, is highly crystalline (> 65%)[21–23] and recalcitrant[24,25]. Nevertheless, microorganisms play a central role in α-chitin remineralization, utilizing it as both a carbon and nitrogen source[26,27], making chitin decomposition an important but understudied component of hadal biogeochemical cycling.

Microbial chitin degradation proceeds through two principal enzymatic routes: hydrolytic cleavage of glycosidic bonds by chitinases[28], and oxidative disruption of the crystalline chitin matrix by lytic polysaccharide monooxygenases (LPMOs)[29]. LPMOs are primarily peroxygenases, relying on a catalytic copper center to activate H_2O_2 as a cosubstrate[30]. Glycosidic bond cleavage therefore depends on H_2O_2 regardless of whether it is supplied externally, since in reactions containing only O_2 and a reductant, H_2O_2 can be generated *in situ* by LPMO oxidase activity or by abiotic oxidation of the reductant[31]. Current evidence for chitin degradation by hadal microorganisms is largely limited to chitinase activity for the hydrolysis process, which has been demonstrated in a few pure-cultured strains[32–35], like *Pseudomonas fluorescens* KT_2_4[32] and piezophile *Photobacterium profundum* SS9[35]. In the transcriptomic analysis[36,37], the piezotolerant fungus *Purpureocillium lilacinum* FDZ8Y1 upregulated chitinase expression under HHP. However, LPMOs, which are recognized

1. State Key Laboratory of Microbial Metabolism, International Center for Deep Life Investigation (IC-DLI), School of Life Sciences and Biotechnology, Shanghai Jiao Tong University, Shanghai, China. 2. Yazhou Bay Institute of Deepsea Science and Technology, Hainan Research Institute, Shanghai Jiao Tong University, Sanya, Hainan, China. 3. Shanghai Changxing Ocean Laboratory, Shanghai Jiao Tong University, Shanghai, China. 4. Institute of Systems and Physical Biology, Shenzhen Bay Laboratory, Shenzhen, Guangdong, China. #These authors contributed equally to this work. *Correspondence: Weishu Zhao (zwsh88@sjtu.edu.cn), Xiang Xiao (zjxiao2018@sjtu.edu.cn)
Received: May 12, 2026; Accepted: October 31, 2026; Published: November 23, 2026

as key factors in the enzymatic conversion of recalcitrant polysaccharides[38] by initiating depolymerization[39,40], have not, to our knowledge, been reported from hadal environments, leaving the oxidative route of chitin decomposition entirely unexplored under hadal high-pressure conditions.

Addressing this gap is technically challenging. Up to 99% of hadal microorganisms remain uncultured and about 90% represent novel species[1,2], meaning that culture-based studies capture only a fraction of hadal microbial diversity and cannot rule out the occurrence of oxidative chitin degradation under HHP. This necessitates culture-independent and community-level approaches[41–44], yet linking broad metabolic signals to specific enzyme activities, particularly for functionally uncharacterized proteins in such extreme environments, remains challenging[45]. Even when candidate enzymes can be identified, resolving their catalytic mechanisms under *in situ* pressure adds a further layer of difficulty, as HHP may fundamentally alter enzyme kinetics and reaction pathways in ways that cannot be predicted from atmospheric-pressure characterization alone[46–49]. Together, these challenges have left it unclear whether oxidative chitin decomposition occurs in hadal environments, which enzymes mediate it, and how HHP changes its rate and mechanism.

In this study, we investigated the effects of HHP on microbial chitin degradation using sediments from the Mariana and Yap Trenches (6–11 km depth) supplemented with α-chitin of 67% crystallinity as the sole carbon and nitrogen source (Supplementary Fig. S1a), a recalcitrant substrate on which LPMO-mediated oxidative attack is expected to be particularly relevant[50,51]. By integrating chitin characterization, metagenomics, metaproteomics, metabolomics, and enzymatic characterization, we directly address how HHP shapes microbial chitin decomposition and its underlying enzymatic mechanism. We show that HHP enhances crystalline chitin decomposition, with AA10-family LPMO-mediated oxidative cleavage identified as the critical enzymatic process. Importantly, we identify Meer1P and Meer2P—two previously functionally unknown enzymes—as the first AA10 LPMOs characterized from hadal microbiomes, and demonstrate that their chitin-oxidizing activities are substantially stimulated by H_2O_2 under HHP. This H_2O_2-responsive activity, together with HHP-induced oxidative stress in microbial cells, provides a key enzymatic mechanism for pressure-accelerated chitin turnover in the hadal biosphere.

RESULTS

Hadal sediment sampling and pressure-gradient cultivations

To test the capacity of hadal microorganisms to utilize highly crystalline chitin, we used the human-occupied vehicle (HOV) to sample sediments from the Mariana Trench and Yap Trench (Fig. 1a). Among them, four sites corresponding to dive FDZ074 (~6 km), FDZ072 (~9 km), FDZ070 (~11 km) from the Mariana Trench, and FDZ060 (~9 km) from the Yap Trench represented natural oligotrophic hadal environments. As a comparison, one site from dive FDZ062 (~8 km) was collected adjacent to an artificially placed dolphin carcass, representing an elevated organic matter input, which reflected the heterogeneity of organic matter inputs characteristic of hadal ecosystems[52–54]. During sampling, we observed active hadal amphipods in the trench (Fig. 1b), providing visual evidence of chitin-bearing fauna in the hadal zone.

To minimize decompression effects during sample recovery, we immediately performed on-deck cultivation of these sediment samples under controlled pressure conditions, using crystalline α-chitin flakes as the sole carbon and nitrogen source (Fig. 1c; Supplementary Fig. S1a). Parallel cultures were carried out under *in situ* high hydrostatic pressure (HHP; 60–115 MPa) and atmospheric pressure (AP; 0.1 MPa) for comparative analysis (Fig. 1c; Supplementary Table S1). To confirm the role of microorganisms in chitin decomposition, microbe-free cultures containing chitin under HHP conditions (HHP-no-microbe + chitin) were included as abiotic controls (Supplementary Table S1). To further assess whether chitin drove microbial activity, sediment cultures without chitin under HHP (HHP-no-chitin) and AP conditions (AP-no-chitin) were used as chitin-free controls (Supplementary Table S1). As chitin mineralization rates in cold deep waters are estimated to be approximately 10-fold slower than at surface temperatures (~25 °C)[55], we cultivated all samples for 18 months at *in situ* temperature (~4 °C) to allow sufficient time for microbial chitin processing under these experimental conditions (Fig. 1c).

HHP accelerates crystalline chitin decomposition by hadal microorganisms

To assess microbial chitin degradation after cultivation, we characterized the surface morphology of recovered chitin fragments by scanning electron microscopy coupled with energy-dispersive spectroscopy (SEM-EDS) (Fig. 1d; Supplementary Fig. S1b; **MATERIALS AND METHODS**). Relative to untreated chitin flakes, those recovered from all AP + chitin and HHP + chitin cultures exhibited clear surface deterioration, confirming that hadal microorganisms can degrade crystalline chitin under both pressure conditions. Notably, surface damage was more severe in HHP + chitin cultures than in their AP counterparts (Fig. 1d; Supplementary Fig. S1b), suggesting enhanced microbial chitin degradation under high pressure. Comparison with HHP-no-microbe + chitin controls, which showed minimal surface alteration, further confirmed that the observed deterioration was microbially driven rather than a direct effect of high pressure alone (Supplementary Fig. S1b).

To quantify chitin depletion, we fluorescently stained and imaged homogenized cultures and measured chitin-flake abundance and mean surface area per flake across all treatments, which were initiated with identical chitin inputs (Fig. 1e–g; **MATERIALS AND METHODS**). Chitin flakes were markedly sparser in HHP + chitin cultures than in HHP-no-microbe + chitin controls, consistent with microbially driven depletion under high pressure (Fig. 1e; Supplementary Fig. S1c). Excluding FDZ062—collected adjacent to an artificially placed dolphin carcass as an organic matter input condition—the remaining ten HHP + chitin cultivations from four oligotrophic dives contained substantially fewer flakes than their AP + chitin counterparts, indicating greater chitin consumption under high pressure (Fig. 1e; Supplementary Fig. S1c).

Chitin-flake counting further supported these observations. In HHP + chitin cultures, chitin-flake abundance declined by 74.3%–98.8% relative to HHP-no-microbe + chitin controls

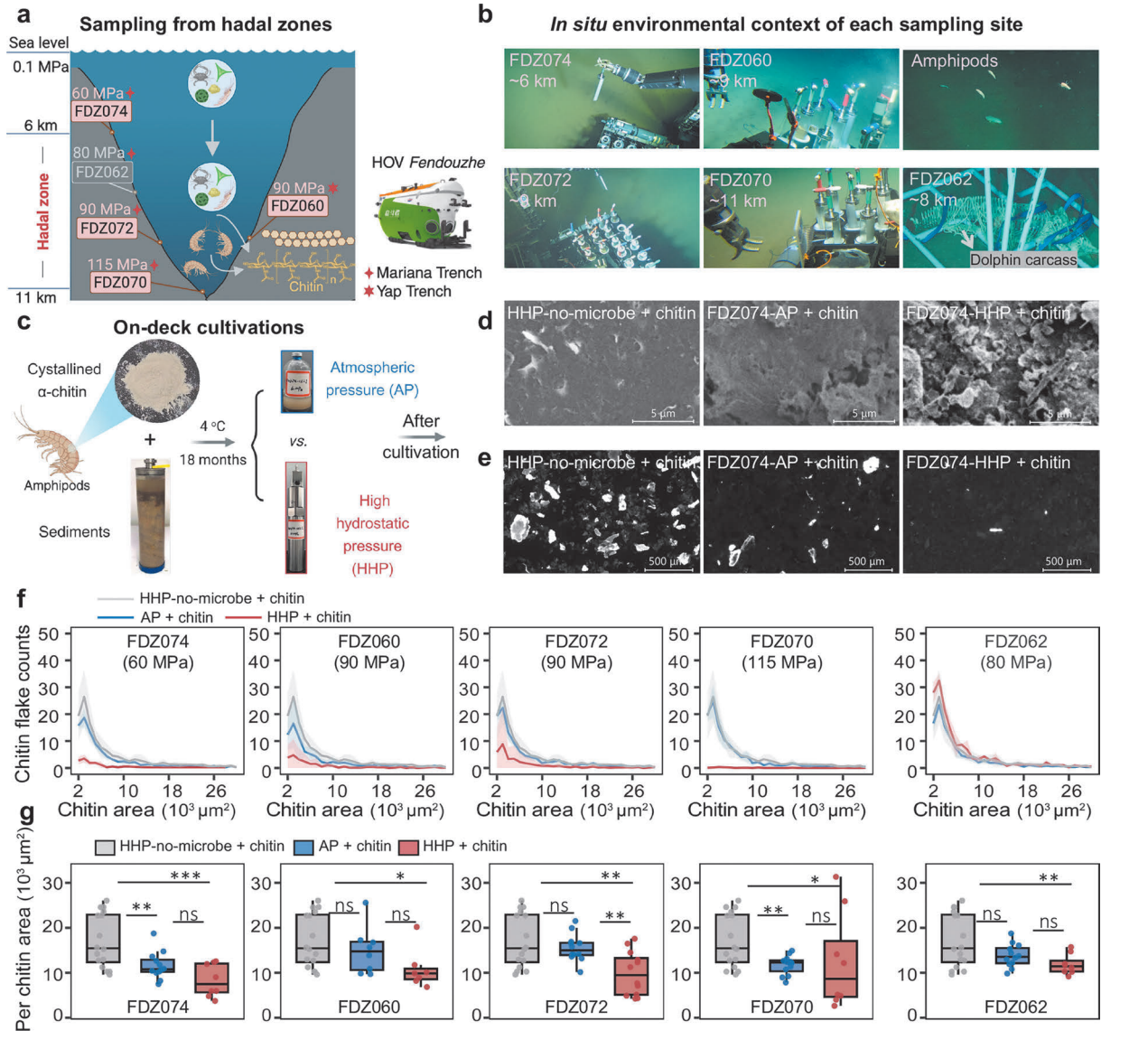

Fig. 1 Hadal sediment sampling, crystalline α-chitin-based cultivations, chitin characterization and quantification. a Sampling of trench sediments using the human-occupied vehicle (HOV), spanning the full depth of the hadal zone, at sites including the Mariana and Yap Trenches. **b** *In situ* environmental context of each sampling site. **c** The sediment cultivation experiments were performed on deck with crystalline α-chitin flakes as the sole carbon and nitrogen source under *in situ* high hydrostatic pressures (HHP; 60–115 MPa) and atmospheric pressure (AP; 0.1 MPa) at 4 °C for 18 months. **d, e** Imaging analyses of chitin flakes in AP + chitin and HHP + chitin cultures and corresponding HHP-no-microbe + chitin controls (using sediments from FDZ074 as an example). Chitin-flake surface morphology was analyzed by scanning electron microscopy coupled with energy-dispersive spectroscopy (SEM-EDS) **(d)** and Calcofluor White-stained chitin flakes by upright fluorescence microscopy **(e)**. **f, g** Chitin quantification of the fluorescence micrographs in **e**, showing flake numbers across surface-area ranges **(f)** and the mean surface area per chitin flake **(g)**. Statistical significance was assessed using Welch's *t*-test on individual microscopic fields of view (*$p < 0.05$; **$p < 0.01$; ***$p < 0.001$; ns, not significant). The numbers of analyzed microscopic fields of view (HHP-no-microbe + chitin/AP + chitin/HHP + chitin) were n = 16/12/8 for FDZ074, 16/8/8 for FDZ060, 16/12/12 for FDZ072, 16/12/12 for FDZ070, and 16/12/8 for FDZ062. The HHP-no-microbe + chitin control was generated by pooling fields of view from no-microbe controls across the available pressure-gradient treatments and is shown as a shared control dataset in each panel.

across the four oligotrophic dives (FDZ074, FDZ060, FDZ072, and FDZ070), whereas only two AP + chitin cultures showed detectable depletion (34.8%–40.8%) (Fig. 1f). Even in the nutrient-enriched FDZ062-HHP + chitin cultures, flake counts did not decrease significantly, yet median flake surface area was reduced by 26.1% relative to the abiotic control, suggesting active but early-stage decomposition (Fig. 1g). Across all HHP + chitin cultures from five sampling dives, median flake surface areas (7,490.1–11,423.4 µm^2) were consistently smaller than those in AP + chitin cultures (10,793.3–14,984.6 µm^2), indicating more advanced fragmentation under high pressure (Fig. 1g).

Collectively, these results demonstrate that hadal microorganisms actively decompose crystalline chitin under both atmospheric and high-pressure conditions, but that decomposition is substantially faster under HHP, as reflected by greater flake depletion and more advanced fragmentation across all HHP cultures.

HHP promotes both oxidative and hydrolytic microbial chitin metabolism

To characterize the chemical changes induced by microbial activity, we analyzed residual chitin fragments from representative HHP + chitin and AP + chitin cultures by micro-Fourier transform infrared (micro-FTIR) spectroscopy (Fig. 2a; **MATERIALS AND METHODS**). Relative to untreated chitin, both HHP and AP cultures showed collapse of glycosidic-linkage peaks (νC–O and ν_{as}C–O–C: ~1,026, 1,072, 1,114, and 1,155 cm^{-1}) into a featureless band, while the N–H (~3,265 cm^{-1}) and O–H (~3,441 and ~3,480 cm^{-1}) stretching bands broadened into shoulders (Fig. 2a). Together, these spectral changes indicate disruption of glycosidic linkages and reduced crystalline order in the residual chitin, consistent with active microbial attack on the chitin backbone under both pressure conditions.

To identify the products of chitin depolymerization, we performed untargeted LC-MS/MS metabolomics on

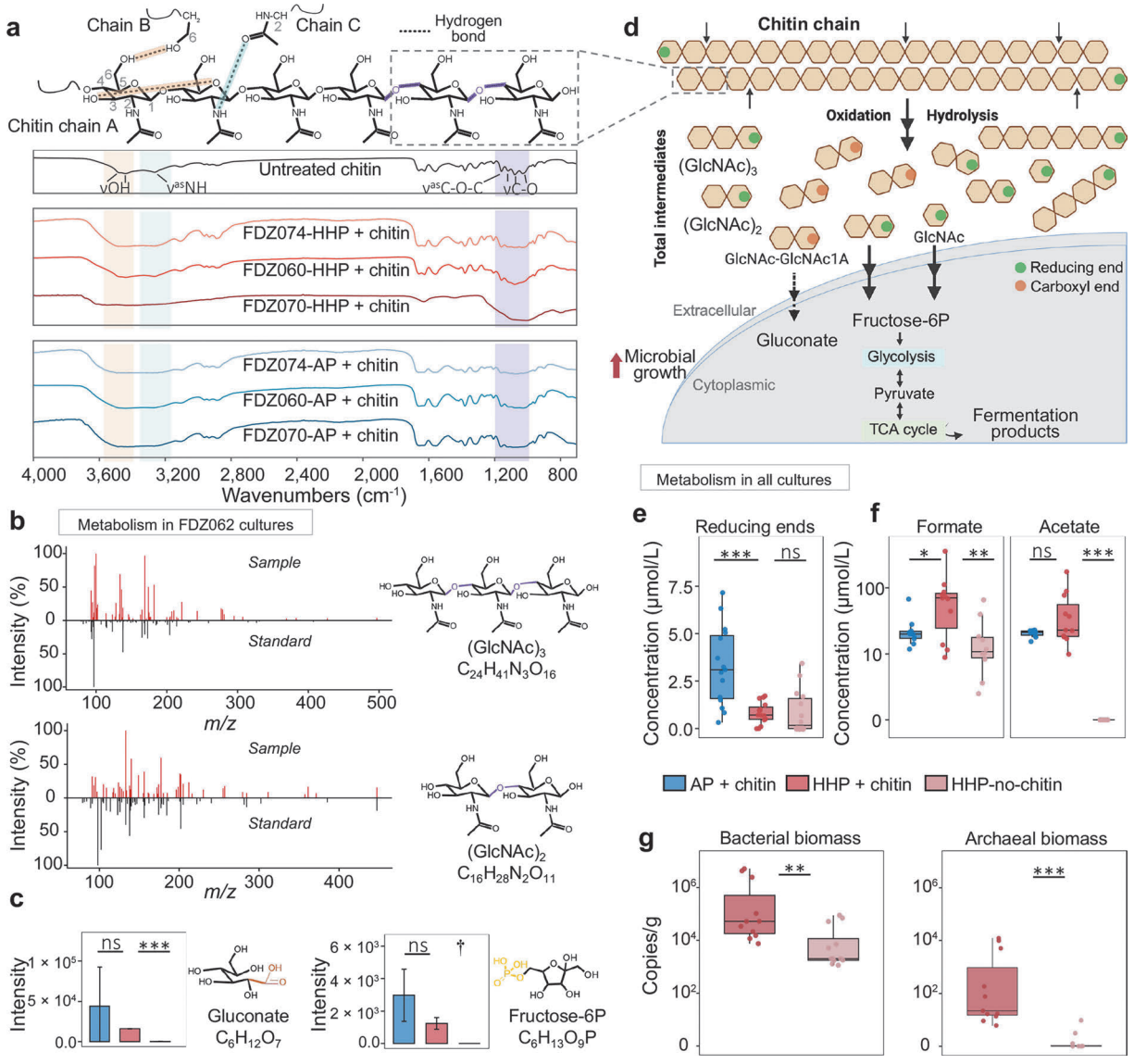

Fig. 2 HHP promotes both oxidative and hydrolytic microbial chitin metabolism. a micro-FTIR spectroscopy of untreated chitin flakes and chitin flakes in HHP + chitin and AP + chitin cultures. **b** Untargeted LC-MS/MS identification of $(GlcNAc)_3$ and $(GlcNAc)_2$ in FDZ062 cultures validated against authentic standards. Culture-derived spectra are shown in red and standard spectra in black. **c** Peak intensities of gluconate and fructose-6-phosphate (fructose-6P) detected in FDZ062 cultures using untargeted LC-MS/MS (n = 3). † indicates fructose-6P detected only in HHP + chitin cultures relative to HHP-no-chitin controls. **d** Schematic illustration of chitin depolymerization through oxidative and hydrolytic cleavage of glycosidic bonds, generating reducing sugars (mixed chitooligosaccharide products) as the major intermediate products, followed by microbial conversion of these intermediates into organic acids as fermentation products, while the overall degradation process supports the growth of microbial biomass. **e** Quantification of the total reducing ends of mixed chitooligosaccharide products (n = 14 for HHP-no-chitin and n = 15 each for AP + chitin and HHP + chitin). **f** Quantification of formate and acetate. n = 10, 10, and 11 for HHP-no-chitin, AP + chitin, and HHP + chitin, respectively. **g** The bacterial and archaeal 16S rRNA gene copy numbers of HHP-no-chitin controls (n = 12) and HHP + chitin (n = 11). For **f** and **g**, data visualization was performed using $\log_{10}$-transformed values, while the y-axis tick labels are shown on the original-value scale for readability. Statistical significance was assessed using Welch's t-test in **c** and **e–g**; for **f** and **g**, Welch's t-test was performed on $\log_{10}$-transformed values (*p < 0.05; **p < 0.01; ***p < 0.001; ns, not significant).

supernatants from FDZ062 HHP + chitin and AP + chitin cultures, using corresponding HHP-no-chitin cultures as controls. FDZ062 was selected because it represented an early stage of chitin decomposition, making it particularly suitable for capturing chitin-derived intermediates before their rapid downstream turnover (Fig. 2b, c; **MATERIALS AND METHODS**). Screening for features enriched by a fold change (FC) ≥ 2 in HHP + chitin cultures relative to the HHP-no-chitin controls identified two hydrolytic depolymerization products, $(GlcNAc)_3$ and $(GlcNAc)_2$, validated against authentic standards (Fig. 2b; Supplementary Fig. S2a), and two downstream metabolites, gluconate and fructose-6P, assigned by accurate mass matching against the Human Metabolome Database (HMDB)[56] (mass error < 3 ppm; isotope similarity > 90%) (Fig. 2c). The enrichment of $(GlcNAc)_3$ and $(GlcNAc)_2$ confirms hydrolytic glycosidic bond cleavage under both pressure conditions (Fig. 2d; Supplementary Fig. S2a). Notably, gluconate was strongly enriched in HHP + chitin cultures (FC = 82.0; Welch's *t*-test, $p < 0.001$), pointing to an additional oxidative decomposition route (Fig. 2c, d). Gluconate is structurally analogous to 2-(acetylamino)-2-deoxy-D-gluconic acid (GlcNAc1A), the oxidized chitin terminus generated by LPMO-mediated C1 oxidation[57] (Supplementary Fig. S2b); gluconate itself is also a key intermediate of the Entner–Doudoroff pathway, suggesting that oxidative cleavage of chitin glycosidic bonds occurred in these cultures. The exclusive detection of fructose-6P in HHP + chitin cultures further confirmed active intracellular assimilation of chitin-derived sugars (Fig. 2c).

To quantify the downstream fate of chitin-derived intermediates, we measured the total reducing ends of mixed chitooligosaccharide products and fermentation products (i.e., formate, acetate, propionate, butyrate, valerate, and lactate) across all cultures (Fig. 2d–f; Supplementary Fig. S2c; **MATERIALS AND METHODS**). Reducing-end (soluble chitooligosaccharide products) concentrations were significantly lower in HHP + chitin cultures (mean 0.8 μmol/L) than in AP + chitin cultures (mean 3.3 μmol/L; Welch's *t*-test, $p < 0.001$), indicating more rapid turnover of chitin-derived sugars into downstream metabolism under high pressure (Fig. 2e). Consistently, formate and acetate, the dominant products jointly accounting for > 90% of the total fermentation products, accumulated to significantly higher levels in HHP + chitin than in HHP-no-chitin controls (Welch's *t*-test, $p < 0.05$; Fig. 2f; Supplementary Fig. S2c). In addition, formate concentrations were significantly higher under HHP (mean 82.9 μmol/L) than under AP (mean 22.9 μmol/L; Welch's *t*-test, $p < 0.05$), while acetate showed a similar trend (mean 46.8 *vs.* 19.4 μmol/L), together indicating that high pressure accelerates the funneling of chitin-derived intermediates into fermentative metabolism (Fig. 2f).

To confirm whether chitin utilization supported microbial growth, we quantified bacterial and archaeal abundances by qPCR (Fig. 2g; **MATERIALS AND METHODS**). Bacterial abundances were significantly higher in HHP + chitin cultures than in HHP-no-chitin controls (mean 1.1×10^6 *vs.* 1.9×10^4 copies per gram; ~58-fold; Welch's *t*-test, $p < 0.01$). Archaeal responses were even more striking: abundances reached up to 2.5×10^3 copies per gram in HHP + chitin cultures, while remaining close to the detection limit in HHP-no-chitin controls (Welch's *t*-test, $p < 0.001$; Fig. 2g). These results confirm that crystalline chitin served as an effective carbon and nitrogen source supporting microbial growth under hadal pressure, with both hydrolytic and oxidative pathways contributing to its decomposition and utilization.

HHP reshapes microbial community structure and favors the chitin oxidative pathway

To investigate the mechanisms underlying enhanced chitin decomposition under HHP, we performed metagenome-guided metaproteomic analyses comparing HHP + chitin and AP + chitin cultures (Fig. 3; **MATERIALS AND METHODS**). Active microbial communities differed markedly between the two conditions (Fig. 3a, Supplementary Table S2). Under HHP, community composition was more variable among samples and less diverse overall, with individual samples dominated by distinct taxa, including Rhizobiales, Enterobacterales, Rhodobacterales, or Parvibaculales, each reaching 60.9%–78.5% relative abundance. By contrast, AP + chitin cultures were more compositionally consistent, dominated by Pseudomonadales, Rhizobiales, and Sphingomonadales. Notably, Nitrososphaerales, the only active archaeal lineage detected, representing ammonia-oxidizing archaea (AOA), showed higher relative abundance under HHP than AP (FC = 2.7), suggesting a potential link between chitin-derived ammonia release and archaeal ammonia oxidation under high pressure. Together, these findings indicate that HHP markedly reshapes the composition of chitin-enriched microbial communities.

Metaproteomic annotation identified 20 enzymes predicted by DeepLocPro[58] to localize to extracellular, periplasmic, or cytoplasmic compartments, collectively supporting stepwise chitin depolymerization, transport, and intracellular utilization (Fig. 3b). Comparison between HHP + chitin and AP + chitin cultures revealed 14 differentially expressed enzymes, including 7 uniquely expressed and 7 overexpressed (FC ≥ 4) under HHP, spanning both extracellular depolymerization and intracellular sugar utilization (Fig. 3c; Supplementary Table S3).

Extracellular chitin depolymerization was enhanced under HHP through both hydrolytic and oxidative routes (Fig. 3b, c). For the hydrolytic process, Chitinase and Endo_I were overexpressed under HHP (FC = 14.0–48.7), consistent with accelerated hydrolytic cleavage of chitin glycosidic bonds. More strikingly, the oxidative route showed a distinctly HHP-associated expression pattern. Two groups of extracellularly secreted enzymes, GbpA and CpbD, were automatically annotated as carbohydrate-binding proteins but refined here as AA10-family LPMO-like enzymes based on amino acid sequence analysis (Supplementary Fig. S3a), indicating their putative chitin-oxidizing functions. Among these oxidative enzymes, GbpA was uniquely expressed under HHP, whereas CpbD was overexpressed (FC = 4.2), with both absent or only weakly detected under AP (Fig. 3c), suggesting an HHP-favored oxidative attack on crystalline chitin. Together, these findings suggest that oxidative and hydrolytic enzymes acted synergistically[39,40] under HHP. HHP-enhanced AA10 LPMO-like enzymes oxidatively disrupted the crystalline chitin matrix, thereby facilitating subsequent hydrolytic cleavage by Chitinase and Endo_I, and collectively accelerating extracellular chitin depolymerization into soluble chitooligosaccharides (Fig. 3b).

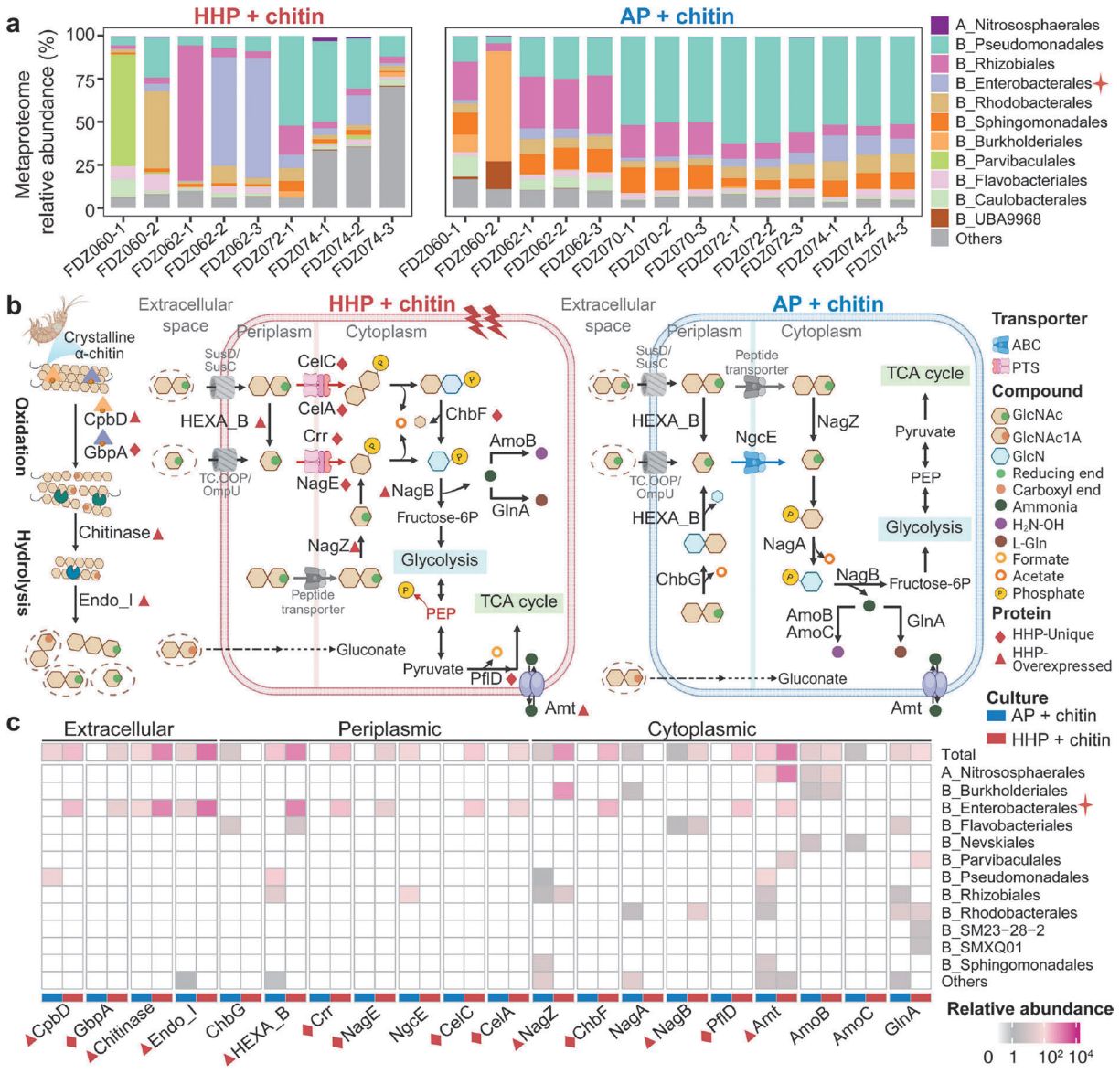

Fig. 3 Metaproteomic evidence for enhanced microbial chitin decomposition and utilization under HHP. a Composition of the active taxa in HHP + chitin and AP + chitin cultures revealed by metaproteomics. **b** Metaproteome-based reconstruction of chitin decomposition and utilization pathways in HHP + chitin and AP + chitin cultures. **c** Comparison of the total relative abundances and order-level taxonomic distributions of enzymes involved in extracellular, periplasmic, and cytoplasmic steps of chitin decomposition and utilization pathways between HHP + chitin and AP + chitin cultures. The red asterisks in **a** and **c** indicate the key order mediating chitin decomposition under HHP.

Additionally, the enhanced depolymerization under HHP was coupled to more efficient intracellular sugar utilization (Fig. 3b, c). The overexpressed hexosaminidase (HEXA_B; FC = 6.2) supported periplasmic conversion of $(GlcNAc)_2$ to GlcNAc, while a phosphoenolpyruvate: carbohydrate phosphotransferase system (PTS; components CelC, CelA, Crr, and NagE), uniquely expressed under HHP, enabled energy-efficient coupled transport and phosphorylation of $(GlcNAc)_2$ and GlcNAc, bypassing the ATP cost of ATP-binding cassette (ABC) transporter-mediated import used under AP. The overexpressed cytoplasmic hydrolases NagZ (FC = 17.1) and uniquely expressed ChbF further processed transported substrates into GlcNAc and glucosamine-6-phosphate (GlcN-6P), which fed into the central metabolism. Downstream, overexpressed GlcN-6P deaminase (NagB; FC = 23.1) catalyzed the release of ammonium from GlcN-6P, consistent with significantly elevated ammonium concentrations in HHP + chitin cultures (Supplementary Fig. S2d), while pyruvate formate-lyase (PflD), uniquely expressed under HHP, accounted for the significantly higher formate accumulation observed under high pressure (Fig. 2f). The overexpression of the ammonium transporter Amt (FC = 8.5) suggests that chitin-derived ammonia may be actively channeled into nitrification or assimilation, potentially linked to the greater AOA activity observed under HHP (Fig. 3a).

The functional specialization observed under HHP was mirrored by taxonomic consolidation. Under HHP, Enterobacterales, primarily a *Shewanella* species (a genus that includes some of the best-characterized deep-sea piezophiles[59]) contributing to extracellular depolymerization and a *Moritella* species (likewise a characteristic deep-sea genus[60]) contributing to transport and intracellular

processing, dominated nearly all steps of the chitin degradation pathway (Fig. 3c; Supplementary Fig. S3b and Table S4), with genus-level analysis further resolving this division of labor (Supplementary Fig. S3b). In contrast, chitin degradation under AP was mainly distributed across three orders, where Pseudomonadales and Enterobacterales shared extracellular depolymerization functions, whereas Rhizobiales contributed to periplasmic processing and ABC transport (Fig. 3c; Supplementary Fig. S3b). This taxonomic consolidation under HHP suggests that high pressure selects for a smaller set of HHP-adapted taxa with specialized but complementary roles, organizing HHP-enhanced chitin decomposition as a cooperative community process.

Collectively, these metagenome-guided metaproteomic results reveal that HHP enhances chitin decomposition through stronger expression of both oxidative and hydrolytic extracellular enzymes. Notably, the GbpA-group AA10 LPMO-like oxidative enzymes were uniquely expressed under HHP, highlighting an HHP-favored oxidative route of chitin depolymerization. This enhanced extracellular depolymerization was further coupled to more efficient PTS-mediated substrate uptake and streamlined intracellular processing, and these processes were carried out by a taxonomically consolidated microbial community.

Hadal AA10 LPMOs are pressure-tolerant chitin-active enzymes

As LPMOs are known to oxidatively disrupt crystalline polysaccharide surfaces that are otherwise poorly accessible to hydrolases[40,51,61], the distinct HHP-associated expression of GbpA and CpbD highlighted their role as key enzymatic factors in rapid crystalline α-chitin decomposition under high pressure (Fig. 3c). We therefore selected Meer1P and Meer2P as representative hadal LPMOs from the GbpA and CpbD groups, respectively, and characterized them directly under hadal conditions. Both LPMOs were obtained by heterologous periplasmic expression in *Escherichia coli* BL21 (DE3), and the purified enzymes were assayed at 4 °C across the full hadal pressure gradient, with the canonical AA10 LPMO CBP21[29] included as a reference (Supplementary Fig. S4a; **MATERIALS AND METHODS**). Under both AP (0.1 MPa) and HHP (60–115 MPa) conditions, Meer1P and Meer2P oxidized the C1 position of crystalline α-chitin, yielding short C1-oxidized chitooligosaccharides (DP2ox to DP6ox; mass difference ~203 Da), identical to those generated by CBP21 (Fig. 4c–e). This result confirms that these hadal-derived LPMOs catalyze oxidative cleavage of crystalline α-chitin under hadal pressure.

The two hadal LPMOs Meer1P and Meer2P differed markedly from the reference CBP21 in how well they tolerated that pressure. To quantify their catalytic activities across the pressure gradient, we treated the reaction products from 6 h assays with the chitobiase SmCHB[62] to convert soluble oxidized products to DP2ox for quantification (Supplementary Fig. S4b–d; **MATERIALS AND METHODS**). Meer1P showed the greatest retention of chitin-oxidizing performance, maintaining 86%–98% of its AP product yield under HHP, while Meer2P retained 77%–95%; in contrast, CBP21 retained only 57%–79% (Supplementary Fig. S4b–d). Thus, the two hadal LPMOs were more tolerant to HHP than the soil-derived LPMO CBP21, consistent with their adaptation to hadal environments.

We next asked what distinguishes these enzymes. Unlike CBP21, phylogenetic analysis identified Meer1P and Meer2P as new members of the GbpA- and CpbD-associated clades, respectively, representing previously uncharacterized LPMOs (Fig. 4a; Supplementary Table S5; **MATERIALS AND METHODS**). AlphaFold3[63] models further showed these LPMOs adopt distinct overall folds, providing a structural basis for comparing their differential responses to high pressure (Fig. 4b; Supplementary Fig. S4e–g). We therefore performed 100 ns molecular dynamics simulations of Meer1P, Meer2P, and CBP21 in their apo and copper-loaded (holo) forms at 25 °C/0.1 MPa, 4 °C/0.1 MPa and 4 °C/80 MPa (Supplementary Fig. S4e–g). Relative to its apo form, holo-Meer1P showed pressure-dependent conformational stabilization at 4 °C/80 MPa, while its CBM73 domain retained comparatively high mobility, consistent with its suggested role in chitin binding[64]. Holo-Meer2P showed low-temperature stabilization that was maintained under high pressure, while also retaining high mobility in its substrate-binding CBM5/12 region. In contrast, holo-CBP21 remained uniformly rigid across all conditions, with several substrate-binding residues showing reduced mobility under high pressure (e.g., His114 and Ile153)[40]. A balance between structural stability and conformational flexibility has been proposed to be important for enzyme function under pressure[65]. Both hadal LPMOs preserve mobility in their substrate-binding regions under high pressure, whereas CBP21 does not (RMSFs of Meer1P and Meer2P are uniformly higher than those of CBP21 in all conditions), and maintain a stable catalytic core, which is consistent with the pressure tolerance observed in the activity assays.

HHP-induced H_2O_2 enhances LPMO-driven chitin oxidation

Having shown that Meer1P and Meer2P remain catalytically active under hadal pressure, we next tested whether H_2O_2 accelerates that activity, as reported for CBP21 and other LPMOs (Supplementary Table S5). All assays were performed at 4 °C (Fig. 4f–h; **MATERIALS AND METHODS**).

Under hadal pressure, H_2O_2 supply directly enhanced chitin oxidation. In 6 h reactions at 60–115 MPa, supplementation with H_2O_2 (50 µmol/L for Meer1P, 30 µmol/L for Meer2P) significantly increased oxidized product yields for both enzymes relative to reactions without exogenous H_2O_2 (Welch's *t*-test, $p < 0.05$; Fig. 4f, g). The same stimulation was observed under AP conditions (Supplementary Fig. S4b, c). H_2O_2 supplementation also modified the pressure response of both Meer1P and Meer2P over the 60–80 MPa range: Meer2P produced fewer oxidized products at 80 than at 60 MPa without added H_2O_2 (mean 5.0 *vs.* 6.1 µmol/L; $p < 0.05$) but more at 80 MPa than at 60 MPa once H_2O_2 was supplied (8.3 *vs.* 7.3 µmol/L; $p < 0.01$; Fig. 4g; Supplementary Fig. S4c), with a similar compensatory response for Meer1P (Fig. 4f; Supplementary Fig. S4b). These results support a role for environmentally available H_2O_2 in driving hadal LPMO-mediated oxidative chitin cleavage under high pressure.

Because hadal high pressure can induce oxidative stress[9,66,67], we examined the H_2O_2 tolerance of hadal LPMOs. Dose–response assays were performed at 4 °C and 0.1 MPa to examine a broad H_2O_2 concentration range of 0–1,000 µmol/L

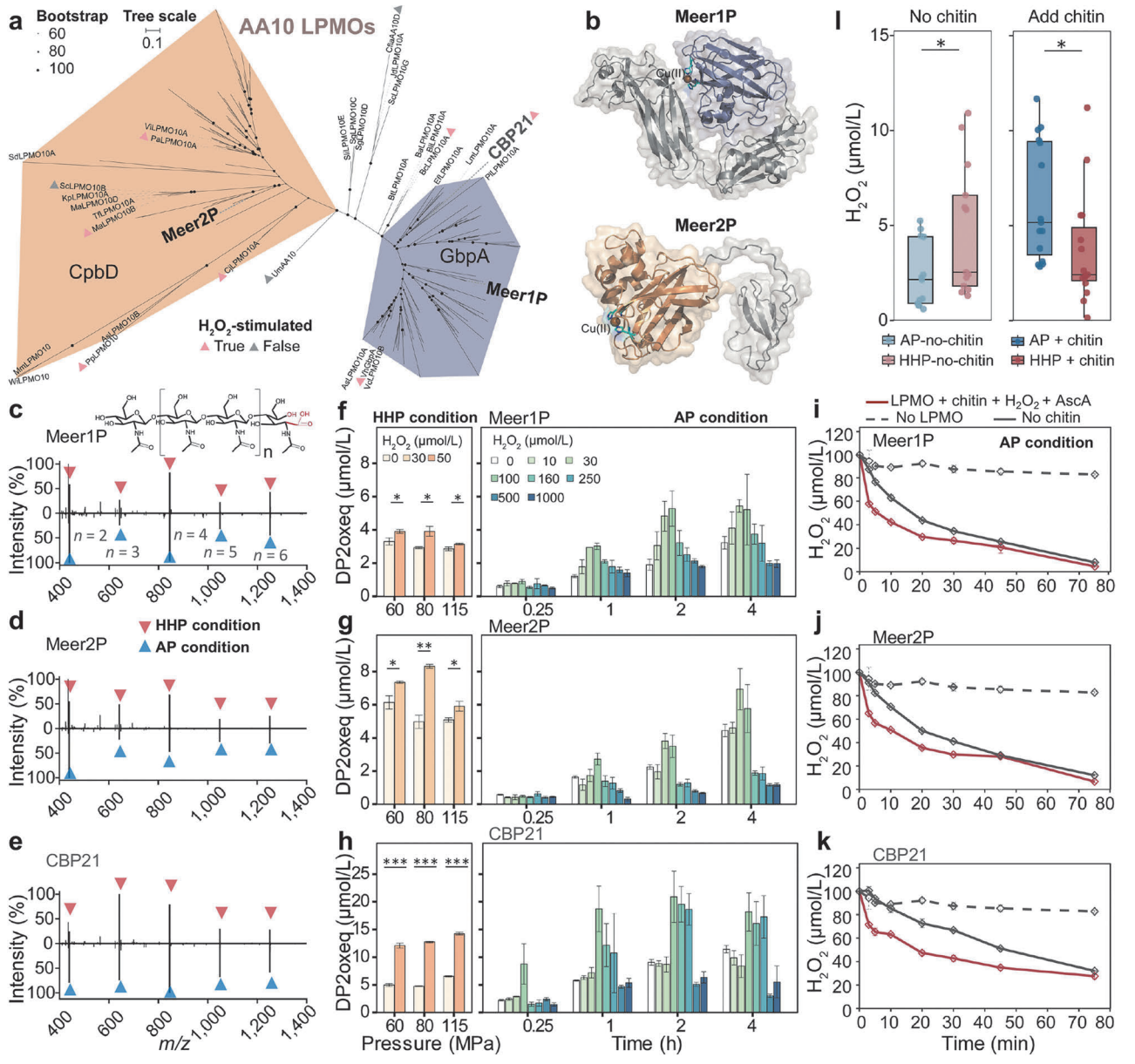

Fig. 4 HHP-induced H_2O_2 stimulates LPMO-mediated oxidative decomposition of crystalline chitin. a Phylogenetic tree of AA10 LPMOs, with experimentally validated enzymes annotated on the tree. **b** Predicted structures of Meer1P and Meer2P generated by AlphaFold3[63]. The AA10 LPMO domains of Meer1P and Meer2P are highlighted in purple and orange, respectively. The catalytic copper ion is shown as an orange sphere, and the histidine-brace residues coordinating the copper ion are shown as blue sticks (His1/His89 in Meer1P; His1/His100 in Meer2P). The full-length Meer1P and Meer2P models had mean pLDDT scores of 90.6 and 86.7, respectively. **c–h** *In vitro* activity assays of Meer1P, Meer2P, and CBP21 were performed at 4 °C under aerobic conditions using 2 mg/mL crystalline α-chitin as the substrate, with 2 μmol/L LPMOs and 100 μmol/L ascorbic acid (AscA) as the reducing agent. **c–e** Negative-mode LC-MS/MS spectra of products generated by Meer1P **(c)**, Meer2P **(d)**, and CBP21 **(e)** under HHP (60–115 MPa; upper spectra) and AP (0.1 MPa; lower spectra) conditions. The detected products were assigned as oxidized chitooligosaccharides from DP2ox to DP6ox, corresponding to degrees of polymerization *n* = 2–6. **f–h** Effects of H_2O_2 on LPMO-mediated chitin oxidation. Left panels show 6 h assays of Meer1P **(f)**, Meer2P **(g)**, and CBP21 **(h)** under HHP conditions (60–115 MPa) with or without exogenous H_2O_2. H_2O_2 was added at 50 μmol/L for Meer1P and CBP21 and at 30 μmol/L for Meer2P. Right panels show time-course assays of Meer1P **(f)**, Meer2P **(g)**, and CBP21 **(h)** under AP conditions (0.1 MPa) in the presence of initial concentrations of exogenous H_2O_2 (0–1,000 μmol/L). Soluble oxidized chitooligosaccharides were converted into DP2ox by treatment with SmCHB and quantified by LC-MS/MS (**MATERIALS AND METHODS**). **i–k** H_2O_2 depletion kinetics of Meer1P **(i)**, Meer2P **(j)**, and CBP21 **(k)** at 4 °C and 0.1 MPa. Reactions contained 2 mg/mL crystalline α-chitin, 2 μmol/L LPMOs, 20 μmol/L AscA, and 100 μmol/L exogenous H_2O_2. Red solid lines indicate complete reactions containing LPMO, chitin, H_2O_2, and AscA. Gray dashed lines indicate no-LPMO controls, and gray solid lines indicate no-chitin controls. Curves show mean values, and error bars indicate SD. Experiments shown in **c–k** were designed with three independent reactions. **l** H_2O_2 concentrations in culture supernatants of AP-no-chitin controls (*n* = 13), HHP-no-chitin controls (*n* = 13), AP + chitin cultures (*n* = 15), and HHP + chitin cultures (*n* = 15). Statistical significance in **f–l** was assessed using Welch's *t*-test. For the HHP assays in the left panels of **f–h**, H_2O_2-supplemented reactions were compared with the corresponding no-H_2O_2 controls under the same pressure condition (*n* = 3), and significance levels are indicated in the panels. For the AP time-course assays in the right panels of **f–h**, the complete *p*-values are provided in **Supplementary Table S6**. For **i–k**, the complete *p*-values are provided in **Supplementary Table S7** (**p* < 0.05; ***p* < 0.01; ****p* < 0.001; ns, not significant).

(Fig. 4f–h; Supplementary Fig. S5a–c and Text S1). Meer1P responded over a broad range of 10–250 µmol/L H_2O_2, with apparent product-formation rates increasing 1.4- to 3.8-fold over the no-H_2O_2 reaction, and sustained an initial apparent rate comparable to the no-H_2O_2 control even at 500–1,000 µmol/L (Fig. 4f; Supplementary Fig. S5a). Meer2P responded over 10–100 µmol/L H_2O_2, with a maximum rate 1.7-fold higher than that of the no-H_2O_2 reaction at 30 µmol/L, and was inhibited at H_2O_2 concentrations of 160 µmol/L or higher, although its activity partially recovered during prolonged incubation (Fig. 4g; Supplementary Fig. S5b). CBP21 was strongly inhibited at 500–1,000 µmol/L H_2O_2, showing lower activity than the no-H_2O_2 control throughout the reaction and reaching a low product plateau within 2 h (mean oxidized product yields, 5.1–6.3 *vs.* 9.0 µmol/L; Welch's *t*-test, $p < 0.05$; Fig. 4h; Supplementary Fig. S5c and Table S6). The particularly broad H_2O_2 tolerance of Meer1P, which maintained initial activity at an H_2O_2 concentration at least twice the concentration that inhibited the soil-derived LPMO CBP21, may represent an adaptation to the oxidative conditions of the hadal zone.

The two hadal LPMOs also showed distinct H_2O_2 utilization patterns compared with CBP21. In depletion assays at 4 °C and 0.1 MPa with 100 µmol/L H_2O_2, H_2O_2 was consumed faster in the presence of chitin than in the corresponding no-chitin reactions for all three LPMOs, indicating H_2O_2 consumption coupled to oxidative chitin decomposition (Fig. 4i–k; Supplementary Fig. S5d–e and Table S7; **MATERIALS AND METHODS**). Notably, Meer1P and Meer2P depleted H_2O_2 markedly faster than CBP21, consuming 35%–42% within the first 3 min versus ~28% for CBP21, with this difference particularly evident in the absence of chitin (Supplementary Fig. S5d–e). Yet, Meer1P and Meer2P showed lower chitin-oxidizing activities than CBP21 at 100 µmol/L H_2O_2 (Supplementary Fig. S5a–c and Text S1). Their H_2O_2 consumption was therefore not fully coupled to productive chitin oxidation, highlighting a more pronounced dual H_2O_2 utilization pattern compared with that of CBP21.

Finally, we returned to the cultivation system to ask whether hadal pressure increases the supply of this co-substrate (Fig. 4l; **MATERIALS AND METHODS**). In the absence of chitin, H_2O_2 concentrations were significantly higher in HHP than in AP cultures (mean 4.7 *vs.* 2.4 µmol/L; Welch's *t*-test, $p < 0.05$; Fig. 4l), consistent with previous reports that high pressure induces oxidative stress in microorganisms[9,66,67]. In the presence of chitin, the pattern was reversed (3.7 *vs.* 6.3 µmol/L; $p < 0.05$; Fig. 4l), indicating that chitin degradation introduced an H_2O_2-consuming process under HHP, consistent with the HHP-associated expression of hadal AA10 LPMOs (Fig. 3c) and their capacity to consume H_2O_2 during oxidative chitin cleavage (Fig. 4i, j). This interpretation is independently supported at the proteome level: relative to AP cultures, HHP + chitin cultures showed increased abundance of multiple proteins involved in aerobic respiration (FC ≥ 4; Supplementary Fig. S6), consistent with altered respiratory redox metabolism and increased electron leakage under high pressure. In parallel, H_2O_2-scavenging enzymes were strongly overexpressed (e.g., FprB, PRDX2_4, and AhpC; 4.7 < FC < 16.0; Supplementary Fig. S6), indicating a cellular response to elevated peroxide stress under HHP. Together, these results support a model in which HHP-induced H_2O_2 accumulation serves as an available co-substrate for hadal LPMOs in the enrichment cultures, stimulating oxidative cleavage and contributing to rapid crystalline chitin decomposition under high pressure.

AA10 LPMOs are preferentially enriched in hadal environments

To assess the potential for LPMO-mediated oxidative chitin processing in the global marine environment, we surveyed 1,098 marine metagenomic samples from 750 geographical locations spanning water depths of 0–11 km, using characterized AA10 LPMO sequences, including Meer1P and Meer2P, as queries and chitinase as a hydrolytic comparator (Fig. 5a; Supplementary Tables S5, S8; **MATERIALS AND METHODS**). Both the detection frequency and the abundance of AA10 LPMO homologs increased with depth and reached their highest values in the hadal zone (Fig. 5a). The proportion of samples in which AA10 LPMOs were detected rose from 49.5% at 0–1 km, through 75.4% at 1–6 km, to 96.0% at 6–11 km, and median TPM values rose correspondingly from 0.5, through 3.7, to 17.2, with hadal abundance significantly exceeding that of both shallower intervals (Fig. 5a; Holm-adjusted pairwise Wilcoxon rank-sum tests, adjusted $p < 0.001$). Chitinase, by contrast, showed no hadal-specific enrichment (Fig. 5a): its detection frequency and median TPM at 6–11 km (99.0% and 37.2) were essentially the same as at 1–6 km (98.6% and 39.8; adjusted $p > 0.05$), although both intervals exceeded the 0–1 km interval (87.3% and 27.5; adjusted $p < 0.05$). This distribution provides ecological context for the H_2O_2-responsive AA10 LPMO pathway identified in our cultivation system, indicating that hadal microbial communities carry a distinctly higher genetic potential for oxidative processing of crystalline chitin, whereas hydrolytic capacity is elevated throughout the deep ocean rather than specifically in the hadal zone.

In summary, by integrating pressure-gradient cultivations, metabolomics, metagenome-guided metaproteomics, and enzymatic characterization, we propose a model in which HHP enhances crystalline chitin decomposition through coordinated oxidative and hydrolytic processing, with H_2O_2-driven AA10 LPMOs acting as a key enzymatic mechanism (Fig. 5b, c). In this model, the H_2O_2 required for LPMO catalysis is supplied by HHP-induced microbial oxidative stress. The global survey indicates that this enzymatic potential is not restricted to our cultivation system: hadal communities retain both the elevated oxidative potential specific to this zone and the hydrolytic potential shared across the deep ocean, whereas shallower communities possess comparable hydrolytic but significantly lower oxidative potential (Fig. 5a, b), consistent with a greater capacity for chitin turnover in the hadal zone.

DISCUSSION

Chitin represents a quantitatively important input of both organic carbon and nitrogen[14] to hadal ecosystems, supplied by sinking marine snow and *in situ* production by amphipods[17–19]. Our results demonstrate that HHP markedly accelerates microbial α-chitin decomposition through coordinated oxidative and hydrolytic processing, with H_2O_2-

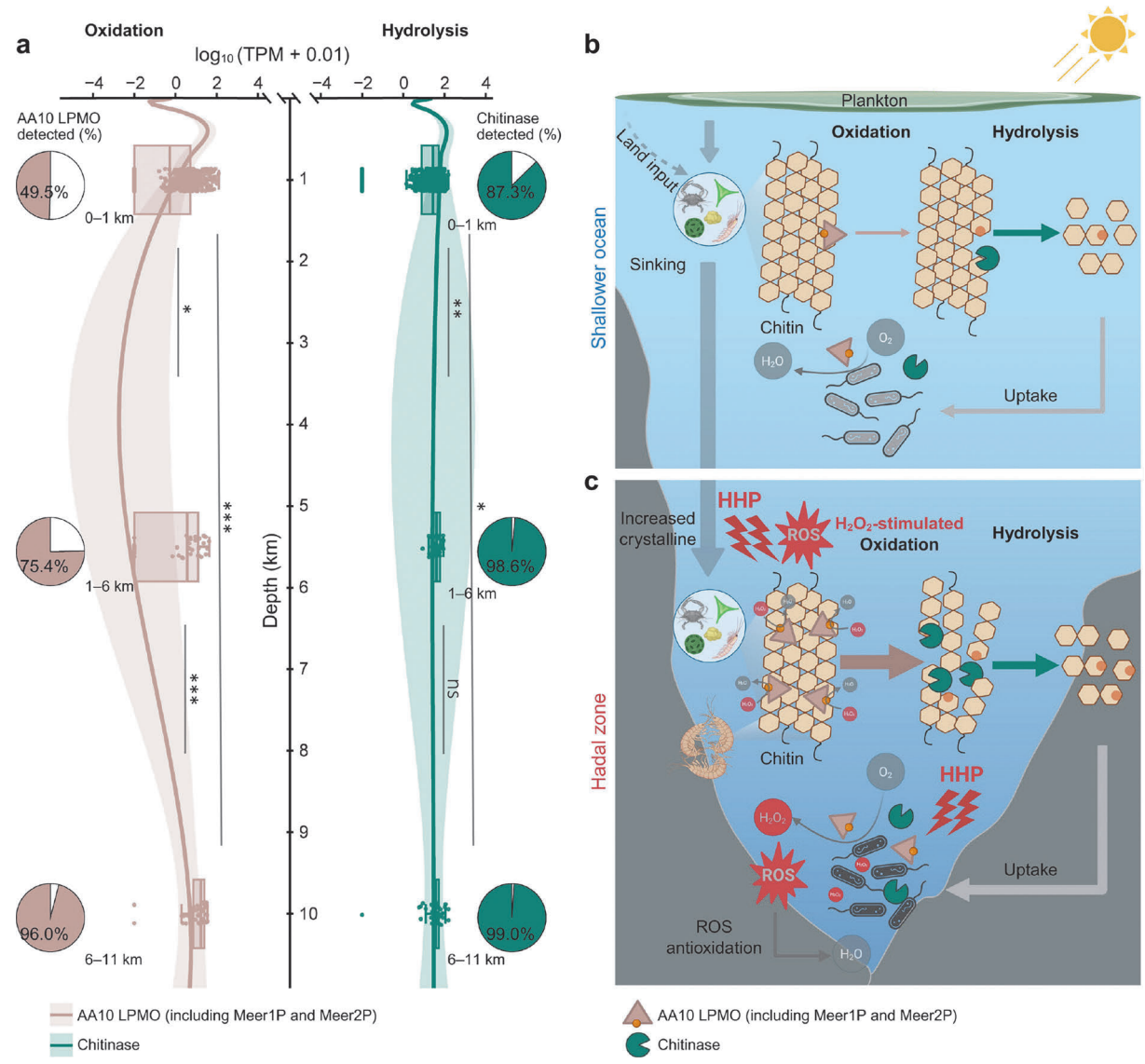

Fig. 5 AA10 LPMOs are preferentially enriched in hadal trenches. a The distribution of AA10 LPMOs and chitinases across the full marine water-depth range, based on 1,098 marine metagenomic samples from 750 geographical locations. Metagenomic datasets were classified into three depth intervals: 0–1 km, 1–6 km, and 6–11 km. Boxplots show the mean TPM at each sampling site (n = 663, 40, and 47 sites, respectively), whereas pie charts show the proportions of metagenomic samples with or without detectable AA10 LPMOs or chitinases. Statistical significance was assessed using pairwise Wilcoxon rank-sum tests, with p-values adjusted using the Holm method (*p < 0.05; **p < 0.01; ***p < 0.001; ns, not significant). **b, c** Proposed schematic of chitin decomposition across the full marine water-depth range. **b** In the shallower ocean, both plankton and potential land input provide chitin, which undergoes mainly hydrolytic decomposition after relatively limited oxidative disruption. **c** In the hadal zone, chitin is supplied by allochthonous inputs from the shallower ocean with increased crystallinity during sinking and by thriving amphipod-dominated macrofaunal communities. Compared with the shallower ocean, the hadal environment showed a markedly higher abundance of AA10 LPMOs. Meanwhile, HHP induces microbial oxidative stress and H_2O_2 production, which can stimulate AA10 LPMO-mediated oxidative depolymerization of crystalline chitin, thereby facilitating subsequent hydrolysis and microbial utilization. Together, these factors may support enhanced chitin degradation in the hadal zone relative to the shallower ocean, making chitin utilization an important component of microbial adaptation to extreme hadal conditions.

driven AA10 LPMO-mediated oxidative cleavage acting as a key enzymatic mechanism. This finding has direct implications for carbon and nitrogen cycling in hadal sediments, because enhanced chitin oxidative degradation is expected to increase C1-oxidized products such as GlcNAc1A[57], with implications for microbial carbon utilization and the downstream flow of chitin-bound carbon and nitrogen. The faster chitin turnover under HHP, driven by enhanced extracellular depolymerization, especially the initial oxidation of the polymer, together with streamlined intracellular processing, suggests that hadal microorganisms have evolved metabolic strategies that exploit extreme pressure rather than merely tolerate it. Although both oxidative and hydrolytic chitin degradation ultimately converge on common fermentation products (e.g., formate, acetate) and ammonia release, enhanced oxidative processing under HHP may shift the balance of these outputs. C1-oxidized chitin termini may be processed through Entner–Doudoroff metabolism, as suggested by the strong enrichment of gluconate in HHP + chitin cultures, rather than solely through the glycolytic route

used for hydrolytic products[68–70]. This metabolic divergence may alter the stoichiometry of organic acid and ammonia production under HHP, with potential consequences for local pH, redox conditions, and nitrogen availability in hadal sediments, where pH has been reported to range from 7.69 to 7.99[71] and O_2 concentrations from approximately 50 to 170 µmol/L[4]. In addition, given that fixed nitrogen loss has been reported in hadal environments[8,9,72,73], pressure-enhanced chitin decomposition and the associated ammonia release may represent an underappreciated source of regenerated nitrogen, supporting archaeal nitrification as suggested by the elevated abundance of ammonia-oxidizing archaea in HHP + chitin cultures. Together, these pressure-modulated shifts in organic acid and ammonia production suggest that HHP does not simply accelerate chitin turnover, but actively reshapes the stoichiometry of carbon and nitrogen remineralization in hadal sediments, with broader implications for benthic nutrient fluxes and the biogeochemical functioning of the deepest ocean.

These potential effects on redox conditions also raise the question of how H_2O_2 availability should be considered in natural hadal environments. Direct H_2O_2 measurements at hadal depths have not, to our knowledge, been reported; concentrations of 4–6 nmol/L have been recorded at 4–6 km and tend to increase with depth below the oxygen-minimum layer[74], and the widespread antioxidant-defense genes and expressed antioxidant enzymes in natural hadal communities[75,76] indicate that hadal microorganisms are exposed to oxidative stress *in situ*. Such bulk measurements, however, describe the averaged state of the surrounding environment rather than the conditions at the sites where enzymes act. Microbial cells continuously generate and consume metabolites in their immediate surroundings, so that the microenvironment around a cell, or around an enzyme bound to a substrate surface, can differ markedly from the bulk phase[77]; this capacity to create local conditions that the bulk environment would not predict is a characteristic feature of living systems. For LPMOs, the relevant quantity is the H_2O_2 available at the chitin surface, which is determined by local production and consumption. LPMO-mediated polysaccharide oxidation can be sustained by a continuous H_2O_2 supply even with little measurable accumulation[38,78,79], and in our cultures the presence of chitin lowered bulk H_2O_2 concentrations under HHP, even though HHP enhanced H_2O_2 accumulation in its absence. The oxidase activity of Meer1P and Meer2P (Supplementary Fig. S7) further suggests that hadal LPMOs may contribute to the H_2O_2 supply at their own reaction sites. Bulk H_2O_2 concentrations, whether measured in natural environments or in culture supernatants, therefore indicate the presence of H_2O_2 and its relative differences between conditions, but cannot be compared quantitatively with the H_2O_2 available to individual enzymes. Accordingly, we interpret the H_2O_2 concentrations in our enrichment cultures as evidence of a pressure-dependent increase in H_2O_2 supply rather than as estimates of *in situ* levels, and the concentrations used in our enzyme assays as a means of defining the catalytic responses and tolerance of the hadal LPMOs. Together with H_2O_2-stimulated chitin oxidation by hadal LPMOs under pressure and the preferential enrichment of AA10 LPMOs in hadal metagenomes (Fig. 5a), these observations support a role for microbial H_2O_2 in LPMO-mediated chitin degradation in the deepest ocean.

The identification and biochemical characterization of Meer1P and Meer2P, the first AA10 LPMOs reported from hadal microbiomes, provide an enzymatic basis for oxidative chitin depolymerization under HHP and, together with the cultivation data, indicate that H_2O_2 supply and consumption are tightly coupled in this system. Meer1P displayed a high level of H_2O_2 tolerance compared with the soil-derived CBP21, a property that has rarely been reported for other characterized bacterial AA10 LPMOs[31,38,80], thereby providing Meer1P with an advantage in exploiting the H_2O_2 available in the hadal environment. Both hadal enzymes also consumed H_2O_2 faster than CBP21 despite slower chitin oxidation, indicating that a substantial fraction of the H_2O_2 they turn over is uncoupled from productive chitin oxidation. This is unlikely to reflect limited H_2O_2 availability, since these comparisons were made in the presence of exogenous H_2O_2 and both hadal enzymes also generated H_2O_2 more rapidly than CBP21 in the absence of substrate (Supplementary Fig. S7). These enzymatic properties help explain the reversal of H_2O_2 levels between chitin-free and chitin-containing cultures noted above. Enhanced generation is therefore not expressed as a higher standing concentration, because consumption rises with it: what high pressure appears to change is not the size of the H_2O_2 pool but the rate at which it turns over, and enzymes able to draw on that flux without being inactivated by it would be favored under such conditions. Whether the uncoupled fraction of H_2O_2 consumption represents a cost of this arrangement or serves an additional function cannot be resolved from the present data, but it is consistent with LPMOs from a rapidly cycling oxidative environment being optimized for something other than the efficiency of each H_2O_2 molecule consumed. Together, these properties support H_2O_2-responsive LPMO-mediated oxidative cleavage as a key enzymatic mechanism contributing to rapid chitin turnover under HHP. Whether other processes contribute comparably to hadal chitin cycling remains an open question; for example, under the elevated oxidative conditions associated with hadal pressure, non-enzymatic processes such as pressure-induced free-radical chemistry may also degrade chitin[81].

Finally, our study demonstrates the power of multi-omics-guided enzyme discovery for accessing the enzymatic potential of microbial dark matter. The vast majority of hadal microorganisms remain uncultured[1,2], and a large fraction carry genes encoding enzymes that are unannotated or incorrectly annotated[82], as illustrated by Meer1P and Meer2P, which were automatically assigned as carbohydrate-binding proteins but functionally reclassified here as AA10 LPMOs. This highlights a fundamental limitation of sequence-based annotation alone for identifying novel enzyme functions in phylogenetically novel microbial lineages prevalent in extreme environments[83,84] such as the hadal zone[82]. The framework demonstrated here, combining pressure-gradient cultivation and community-level multi-omics identification of differentially expressed enzymes with targeted heterologous expression and biochemical validation, provides a tractable and generalizable approach for characterizing novel enzymes from uncultured microorganisms. As long as a metabolic

phenotype is observable at the community level, multi-omics can pinpoint the responsible enzymes for functional validation, offering a broadly useful path toward unlocking the enzymatic potential of Earth's most phylogenetically diverse and least characterized microbial ecosystems.

MATERIALS AND METHODS

Sampling and cultivation

The hadal sediment samples were systematically collected by the HOV *Fendouzhe*, spanning the full water depth range (6–11 km below sea level) in the Mariana Trench: four sites corresponding to dives FDZ074 (~6 km), FDZ062 (~8 km), FDZ072 (~9 km), and FDZ070 (~11 km). We also collected the sediments from dive FDZ060 (~9 km) in the deepest region of the Yap Trench. Within 6 h of sediment sample collection on the seafloor, cultivation experiments were established on board by adding 0.125 g α-chitin derived from shrimp shells (~67% crystallinity; Sigma-Aldrich, Cat#V900332) to each cultivation containing equal amounts of *in situ* sediment and 25 mL filtered seawater. These cultivations were conducted in parallel under *in situ* high hydrostatic pressure (HHP; 60–115 MPa) and atmospheric pressure (AP; 0.1 MPa) at the same *in situ* temperature (4 °C), designated HHP + chitin and AP + chitin, respectively. Chitin-free sediment controls were established under both HHP (HHP-no-chitin) and AP (AP-no-chitin) conditions to evaluate background microbial activity. For the abiotic controls (HHP-no-microbe + chitin), 0.125 g α-chitin was incubated with 25 mL sterile-filtered *in situ* seawater under the corresponding *in situ* pressures: 80 MPa for FDZ062, 90 MPa for FDZ060 and FDZ072, and 115 MPa for FDZ070. All treatments and controls were set up in triplicate, whereas HHP-no-microbe + chitin controls were analyzed together as four independent abiotic replicates.

The *in situ* high hydrostatic pressure cultivations (60–115 MPa) were conducted in customized pressure-retaining tubes, with atmospheric pressure cultivations (0.1 MPa) established in parallel in sealed serum bottles for comparison. Different vessel types were used because HHP incubations required pressure-resistant tubes capable of maintaining 60–115 MPa, as is standard practice in high-pressure microbiology[85–87]. All other cultivation parameters for the AP + chitin and HHP + chitin treatments, including sediment inoculum, substrate, temperature, incubation duration, and sealed conditions, were kept identical. We note that differences in vessel geometry may nevertheless influence mass transfer or substrate–cell contact and should therefore be considered when interpreting AP–HHP comparisons and extrapolating these results to natural hadal sediments.

Quantification of chitin flakes

Fluorescent staining of chitin flakes was performed using a method adapted from a previously reported protocol[88], with some modifications. After cultivation, each culture was homogenized, and 5 mL of culture was collected and freeze-dried overnight. The dried powder from each culture was then thoroughly mixed and transferred into a clean 2-mL centrifuge tube. Subsequently, 2 mL ultrapure water (18.2 MΩ·cm) was added to prepare a suspension. After homogenization, 50 µL of the suspension was transferred onto a glass slide and stained with 2 µL of 1 mg/mL Calcofluor White solution (Sigma-Aldrich, Cat#18909-100ML-F) for fluorescence microscopy observation. The mixture was homogenized and incubated in the dark for 30 min. Images were acquired at 5× magnification. For each sample, four spatially separated fields of view around the slide area were selected and imaged as 5 × 5 tiled images to obtain large-field, high-resolution fluorescence micrographs. The number of chitin flakes and the total surface area of chitin flakes in each fluorescence micrograph were quantified using ImageJ 1.54g[89]. The average surface area per flake was then calculated by dividing the total flake surface area by the corresponding flake number. To exclude potential interference from fungal cells, fluorescent particles with an area smaller than 2,000 μm^2 were excluded from the analysis.

Recovery and characterization of chitin flakes

For each culture, 0.5 mL of the cultivated sample was passed through a standard stainless-steel sieve with a pore size of 63 µm to remove large debris and collect the coarse fraction containing chitin flakes. The coarse fraction was further purified by density separation using $ZnCl_2$ solution. Briefly, 300 g $ZnCl_2$ was dissolved in 200 mL ultrapure water (18.2 MΩ·cm) to prepare a $ZnCl_2$ solution with a density of approximately 1.69 g/cm^3. The coarse fraction was added to the $ZnCl_2$ solution and centrifuged at 8,000 rpm for 10 min at room temperature. After centrifugation, chitin-like flakes were observed suspended in the supernatant. The supernatant was carefully collected and thoroughly rinsed with ultrapure water on a 63 µm sieve to remove residual $ZnCl_2$. The chitin-like flakes retained on the sieve were then collected and freeze-dried for further instrumental analyses.

SEM-EDS. The surface morphology of the recovered chitin flakes was observed using scanning electron microscopy coupled with energy-dispersive spectroscopy (SEM-EDS; RISE-MAGNA, TESCAN). Energy-dispersive spectroscopy was used to determine the elemental composition of carbon, nitrogen, and oxygen in the recovered particles. These elemental profiles were compared with those of the chitin standard to confirm that the observed particles were chitin flakes.

Micro-FTIR. Micro-FTIR measurements on chitin flakes were performed using a Nicolet iN10 MX micro-FTIR spectrometer (Thermo Fisher Scientific) in transmission mode over the spectral range of 700–4,000 cm^{-1}. Each reported spectrum represents the average of at least two spectra measured from different areas of the sample. The carbon dioxide absorption region at 2,200–2,400 cm^{-1} was removed before further analysis.

Reducing ends measurement

Reducing ends in culture supernatants were quantified using a modified 3-methyl-2-benzothiazolinone hydrazone (MBTH) assay[90]. Briefly, 0.2 mL of N-acetyl-D-glucosamine (standard) or culture supernatant was mixed with 0.2 mL of NaOH (0.5 mol/L). Subsequently, 0.2 mL of MBTH-A reagent, prepared by mixing equal volumes of 1 mg/mL DTT solution and 3 mg/mL MBTH solution, was added. The mixture was vortexed and incubated at 80 °C for 15 min in a thermostatic water bath. Immediately after removal from the water bath, 0.4 mL of MBTH-B reagent, containing 0.5%

$FeNH_4(SO_4)_2 \cdot 12H_2O$, 0.5% sulfamic acid, and 0.25 mol/L HCl, was added, followed by vigorous mixing. The reaction mixture was allowed to stand at room temperature for 60 min, after which absorbance at 620 nm was measured using a microplate reader (BioTek) with 200 µL per well.

Organic acids and ammonium concentration measurements

For organic acid analysis, recrystallized 2-nitrophenyl hydrazine (NPH; Sigma-Aldrich, Cat#N21588) was used to prepare a 0.1 mol/L NPH solution by dissolving in 0.25 mol/L HCl. N-(3-dimethylaminopropyl)-N′-ethylcarbodiimide hydrochloride (EDC; CNW Technologies, Cat#XW01708411901) was used to prepare a 0.3 mol/L solution by dissolving in ultrapure water (18.2 MΩ·cm). Equal volumes of redistilled pyridine (Sigma-Aldrich, Cat#33553) and concentrated HCl were mixed to prepare a pyridine buffer. Standards and culture supernatant were treated as follows to obtain the NPH derivatives of the organic acids: to each 0.1 mL sample, 10 µL of pyridine buffer was added and bubbled for 4 min to remove any CO_2. Then 10 µL each of NPH and EDC was added, mixed, and incubated for 1.5 h at room temperature. Following that, 10 µL of 40% (*w*/*v*) KOH was added to each sample, and samples were mixed and incubated at 70 °C for 10 min[91]. Treated standards and samples were analyzed via reversed-phase ultra-high-performance liquid chromatography-mass spectrometry (Waters ACQUITY UPLC-SQD), using an analytical column (4.6 mm × 250 mm). Organic acid concentrations were quantified by comparison with treated standards using retention time and *m*/*z* matching, with peak areas used for calibration-based quantification.

Ammonium concentration was determined based on the Berthelot reaction[92], in which ammonium reacted with phenol (Sigma-Aldrich, Cat#W322318) and sodium dichloroisocyanurate (Sigma-Aldrich, Cat#35915) in the presence of sodium nitroprusside (Sigma-Aldrich, Cat#71778) to form a blue-green complex with a maximum absorbance at 660 nm.

Coextraction of DNA and protein

The 0.5 g pellet of cultivation samples was mixed with 1 g quartz sand (~1 mm diameter), 1 mL sodium dodecyl sulfate (SDS) buffer [1% SDS, 240 mmol/L sodium phosphate buffer (pH 8.0), 20 mmol/L ethylenediaminetetraacetic acid (EDTA), 60% sucrose, 3 mL phenol (Tris-saturated phenol, pH 7.7–8.1, containing 0.1% 8-hydroxyquinoline), 0.06 g dithiothreitol (DTT), and 30 µL protease inhibitor (Halt™ Protease and Phosphatase Inhibitor Single-Use Cocktail, Thermo Scientific)]. Then, the samples were homogenized (4 m/s, 20 s) three times (3 min intervals) with a homogenizer (FastPrep-24, MP Biomedical). After grinding, the tubes were centrifuged (10,000 × *g*, 5 min). The upper organic phase was mixed with five times the volume of methanol-ammonium acetate (0.1 mol/L ammonium acetate dissolved in methanol) and centrifuged (10,000 × *g*, 10 min) after 16 h of incubation at −20 °C. After suspension in 1 mL anhydrous ethanol, the precipitate was transferred to a 1.5 mL centrifuge tube and centrifuged (14,000 × *g*, 5 min). Then, the precipitate was rinsed with anhydrous ethanol again. The protein precipitate was air-dried and finally dissolved in 40 µL of 8 mol/L urea (8 mol/L urea dissolved in 0.1 mol/L Tris-HCl, pH 8.0). Bradford reagent was used to determine the protein concentration.

After the phenol organic phase was removed, 1 mL of hexadecyl trimethyl ammonium bromide (CTAB) buffer [2% CTAB, 1.4 mol/L NaCl, 240 mmol/L sodium phosphate buffer (pH 8.0), 20 mmol/L EDTA, 2% polyvinylpyrrolidone (average mol wt 40,000)], and 1 mL of phenol-chloroform-isoamyl alcohol (PCI) (25:24:1, pH 8.0) were added to the residual system and homogenized (4 m/s, 20 s), followed by centrifugation (10,000 × *g*, 5 min). The upper aqueous phase was mixed with an equal volume of chloroform-isoamyl alcohol (24:1) and centrifuged (10,000 × *g*, 5 min). The upper aqueous phase was mixed with 2 times the sample volume of polyethylene glycol (PEG) solution (30% PEG 6000 dissolved in 1.6 mol/L NaCl) and 20 µg of glycogen (RNase-free), incubated for 2 h at 4 °C, and centrifuged (14,000 × *g*, 10 min). The precipitate was rinsed with 1 mL of cold 75% ethanol, followed by centrifugation (14,000 × *g*, 5 min). Then, the supernatant was carefully aspirated and air-dried. The nucleic acid precipitate was dissolved in Tris-HCl buffer (10 mmol/L Tris-HCl, pH 8.0). The nucleic acid solution was mixed with 20 µg of RNase A (TransGen) and incubated at 37 °C for 30 min, and the DNA was purified using the Genomic DNA Clean & Concentrator-10 kit (ZYMO) according to the manufacturer's instructions.

Enzymatic cleavage of proteins and purification of peptides

Protein (1–10 µg) was diluted to 50 µL with 8 mol/L urea and mixed with 2 µL of 0.5 mol/L DTT, and then incubated at 37 °C for 30 min. Then, the sample was mixed with 5 µL of 0.5 mol/L IAA and incubated for 30 min at room temperature while being protected from light, followed by mixing with 2 µL of 0.5 mol/L DTT. The alkylated protein was combined with 413 µL of 50 mmol/L ammonium bicarbonate buffer (50 mmol/L ammonium bicarbonate dissolved in water), mixed at a ratio of 1:25 (by protein mass) with trypsin/lysyl endopeptidase (Trypsin/Lys-C Mix, mass spectrometry grade, Promega), and incubated for 16 h at 37 °C. The digested sample was mixed with one-third volume of sample buffer (2% trifluoroacetic acid dissolved in 20% acetonitrile) and then centrifuged (14,000 × *g*, 5 min). The supernatant was filtered using a 0.5 mL 10 kDa ultrafiltration filter (Microcon-10 kDa, Millipore) by centrifugation (12,000 × *g*, 40 min), and the filtrate was collected.

The resin of the C18 Spin Columns (Pierce™ C18 Spin Columns, Thermo Scientific) was washed in sequence with 200 µL of 50% methanol and 200 µL of equilibration solution (0.5% trifluoroacetic acid dissolved in 5% acetonitrile). The ultrafiltrate was then added to the C18 spin column, where the peptides were adsorbed by the resin. Afterward, the resin was washed with 200 µL of equilibration solution. The peptides were then eluted from the spin column using 20 µL of 70% acetonitrile. The eluate was gently dried in a centrifugal concentrator, and the peptides were dissolved in 20 µL of 0.1% formic acid. The purified peptides were analyzed using nanoflow liquid chromatography-electrospray ionization tandem mass spectrometry (nLC-ESI-MS/MS) for shotgun proteomics.

Mass spectrometry data acquisition

After assessing sample quality and relative peptide abundance

using a NanoDrop spectrophotometer, 8 µL of peptide solution was injected into the nano-flow liquid chromatography–tandem mass spectrometry (nLC-MS/MS) system, which comprised a nanoElute® liquid chromatography instrument (Bruker) coupled to a timsTOF Pro mass spectrometer (Bruker). Peptides were separated on a reversed-phase C18 analytical column (25 cm × 75 µm ID, APT) with an overall gradient from 2% to 95% acetonitrile at a flow rate of 300 nL/min over 90 min at 60 °C. Data-dependent acquisition (DDA) was performed in PASEF mode (oTOF control v6.0.0.12). The ion mobility window was set to $1/K_0$ start = 0.6 V·s/cm^2 to $1/K_0$ end = 1.6 V·s/cm^2, with a ramp time of 100 ms with a locked duty cycle and a mass range of 100–1,700 *m/z*. MS/MS spectra were acquired with an accumulation time of 2 ms and a cycle time of 100 ms. The target intensity was set at 6,000 and the threshold intensity was set at 200.

Metagenomic data processing, assembly, and binning

Approximately 10 ng of metagenomic DNA was fragmented to ~500 bp for preparation of the DNA libraries. Then, libraries were constructed using the FAST PCR Kit (MGI, BGI) and sequenced on the DNBSEQ-T1 platform with 150-bp paired-end reads. Two libraries were constructed for each sample.

Raw reads from each library were filtered using fastp (v0.23.2)[93] and assembled using MEGAHIT (v1.2.9)[94]. Raw reads were filtered again without merging to generate clean reads for recruitment, which were then mapped to contigs of ≥ 1,000 bp using bbmap.sh (v39.01) to calculate contig coverage[95]. Contigs of at least 2,500 bp were used in binning. Fourteen parallel-binned results for each sample were generated [9 with MetaBAT 2 (v2.15)[96], 2 with MaxBin 2 (v2.2.7)[97], and 1 each with CONCOCT (v1.1.0)[98], VAMB (v3.0.2)[99], and MetaDecoder (v1.0.14)[100]], ensembled using UniteM (v1.2.4) and filtered to retain bins with completeness −5 × contamination ≥ 50 that also passed GUNC (v1.0.5) checks (v1.0.5)[101]. Filtered bins were collected and clustered using dRep (v3.4.0)[102] at 95% ANI, and the representative genome of each cluster was collected as the MAG set used in this study. Clean reads from two libraries of each sample were concatenated and mapped to those representative MAGs with bwa (v0.7.17-r1188)[103] for CoverM (v0.6.1)[104] to calculate the metagenomic relative abundance of MAGs.

Gene annotation and metaproteomic database construction

Coding sequences were predicted from contigs by pyrodigal-gv (v0.3.1)[105,106], and those encoding proteins with length < 33 amino acids were removed. Functional annotation including GO and KEGG was performed by MANTIS (v1.5.5)[107], and the taxonomy of the contig genes was annotated by kaiju (v1.9.2)[108] with a public database (kaiju_db_nr_euk_2022-03-10, downloaded from kaiju.binf.ku.dk). The metagenomic relative abundance of contig genes was calculated as the TPM value by Salmon (v1.9.0)[109]. For metaproteomic database construction, protein sequences shorter than 50 amino acids were removed to improve search performance. Both MAG- and contig-derived genes were included for peptide identification.

Metaproteomic searching, peptide validation, protein inference and quantification

Raw DDA files from three replicate injections of peptides acquired on a timsTOF Pro mass spectrometer (Bruker) were used. The FragPipe platform (v18.0)[110] with MSFragger (v3.5)[111] and Philosopher (v4.4.0)[112] was used to perform decoy generation, searching, peptide validation, and protein inference. Reversed protein sequences were appended to the original databases as decoys for MSFragger. The common repository of adventitious proteins (cRAP, thegpm.org/crap/) was used as a contaminant protein database. For the two-step database search, the initial search was performed with both precursor and fragment mass tolerances set to 40 ppm. Tryptic cleavage specificity was applied, and up to two missed trypsin cleavages were allowed. Isotope error was set to 0/1/2. Peptides with 7–50 amino acids and 500–5,000 Da were considered for identification. The search included variable methionine oxidation, variable protein N-terminal acetylation, and fixed carbamidomethyl cysteine modifications. The maximum number of variable modifications per peptide was set to 3. The peptide-spectrum matches (PSMs) were further rescored using deep learning prediction by the MSBooster[113] module, and discrimination between correct and decoy spectra was performed by Percolator[114]. The validated peptides were assigned either as unique peptides to a particular protein or as razor peptides to a single protein that had the most peptide evidence by ProteinProphet[115]. The results of the first step, including peptides and proteins, were filtered with a 25% false discovery rate (FDR). For the second step of the search, the inferred proteins generated from the first search were used as the database and then subjected to the same parameters, except that they were filtered with a 1% FDR. The MaxLFQ intensity, including unique and razor peptides, was calculated using IonQuant (v1.8.0)[116] with a 1% match-between-run ion FDR and one MaxLFQ min ion. Proteins that matched at least two unique peptides were considered high-confidence identifications and selected for further functional analysis.

Functional and taxonomic assignment of chitin-degrading proteins

Proteins involved in chitin degradation were identified from the metaproteomic datasets based on their functional annotations and assigned to different steps of the chitin degradation pathway. Protein subcellular localization was predicted using DeepLocPro[58]. LPMO-like proteins and chitin hydrolases predicted to act extracellularly on the insoluble chitin were assigned to extracellular depolymerization, whereas transporters and periplasmic or cytoplasmic enzymes involved in the metabolism of soluble products were assigned to intracellular utilization. Correspondingly, microorganisms expressing LPMO-like proteins and chitin hydrolases were operationally classified as degraders, whereas those mainly expressing transporters and intracellular enzymes were classified as consumers, following previous definitions[44,117]. Taxonomic assignments of the corresponding proteins were used to resolve the contributions of different microbial taxa to individual steps of the chitin degradation pathway.

Microbial 16S rRNA gene copy number quantification

Real-time qPCR experiments were performed on an Applied

Biosystems QuantStudio 3 Real-Time PCR System (Applied Biosystems). Bacterial 16S rRNA genes were quantified using primer set bac341f (5′-CCTACGGGWGGCWGCA-3′) and bac519r (5′-TTACCGCGGCKGCTG-3′)[118,119]. Archaeal 16S rRNA genes were quantified using primer set Uni519f (5′-CAGCMGCCGCGGTAA-3′) and Arc908R (5′-CCCGCCAATTCCTTTAAGTT-3′)[120]. For bacterial 16S rRNA gene quantification, the 20 µL reaction mixture contained: 10 µL PowerUp SYBR Green Master Mix (Applied Biosystems, MA, USA), 1.0 µL each of 10 µmol/L forward and reverse primers (Sangon Biotech, Shanghai, China), 1 µL template DNA, and autoclaved double-distilled water to 20 µL final volume. The thermal cycling program consisted of 40 cycles of 95 °C for 30 s, 56 °C for 30 s, and 72 °C for 30 s for bacterial 16S rRNA gene amplification, and 40 cycles of 95 °C for 30 s, 60 °C for 30 s, and 72 °C for 30 s for archaeal 16S rRNA gene amplification. Standard curves were generated for each gene target, with all reactions achieving $R^2 > 0.99$. Ultrapure water (18.2 MΩ·cm) was set as a negative control with undetermined signals while all samples were detectable with amplification signals.

Phylogenetic analysis and distribution of AA10 LPMOs in marine metagenomes

For the phylogenetic analysis of Meer1P and Meer2P, the reference dataset included experimentally verified AA10 LPMO sequences (Supplementary Table S5) and unverified homologs annotated as CpbD and GbpA. The unverified sequences were clustered and deduplicated using CD-HIT (v4.8.1)[121] with a 70% identity threshold. The combined sequence set was aligned using MAFFT (v7.505)[122] with the parameters --genafpair --maxiterate 1000 and then trimmed with trimAl (v1.4.rev15)[123] with the -automated1 parameter. A maximum-likelihood tree was constructed using IQ-TREE (v2.0.3)[124] with the model LG + R5 with 1,000 bootstrap replicates.

For comparisons of AA10 LPMO and chitinase (Supplementary Table S8) sequences across different water layers, samples from publicly available datasets[125] were first assembled into contigs using MEGAHIT (v1.2.9)[94]. Coding sequences (CDSs) were then predicted and translated using Prodigal[106]. Sequence similarity searches were performed using DIAMOND[126] blastp (--evalue 1e-5 --query-cover 50 --ultra-sensitive).

Recombinant enzyme expression, purification, and biochemical characterization

The genes encoding Meer1P, Meer2P, and CBP21 (GenBank accession: AY665558.1) without their signal peptide sequences were ligated into the pET22b vector. The genes encoding chitobiase (SmCHB; GenBank accession: L43594) and chitooligosaccharide oxidase (ChitO; NCBI RefSeq accession: XP_391174.1) without their signal peptide sequences were ligated into the pET28a and pET28a-MBP vectors, respectively, with ChitO N-terminally fused to maltose-binding protein (MBP). The constructed plasmids were then transformed into *Escherichia coli* BL21 (DE3). Recombinant *E. coli* strains were cultured at 37 °C in Lysogeny Broth medium until the OD_{600} reached 0.6–0.8. Protein expression was induced with 0.2 mmol/L isopropyl-β-D-thiogalactopyranoside (IPTG; Sangon Biotech, Cat#A600168), and the cultures were further incubated at 18 °C for 16 h. Cells were harvested by centrifugation. Recombinant Meer1P, Meer2P, and CBP21 proteins carrying a C-terminal His-tag were extracted from the periplasmic fraction by cold osmotic shock and purified using Ni-nitrilotriacetic acid (Ni-NTA) resin (Sangon Biotech, Cat#C600033). Recombinant SmCHB carrying an N-terminal His-tag and ChitO carrying an MBP tag and a C-terminal His-tag were purified using Ni-NTA resin (Sangon Biotech, Cat#C600033).

For biochemical characterization, Meer1P, Meer2P, and CBP21 were first saturated with copper by incubation with a twofold molar excess of $CuSO_4$ at 4 °C for 60 min. Excess copper was removed by desalting the protein solution using PD-10 desalting columns (GE Healthcare). Unless otherwise specified, the standard reaction mixture contained 2 mg/mL crystalline α-chitin, 2 µmol/L Cu^{2+}-saturated LPMO, 100 µmol/L ascorbic acid (AscA), and 10 mmol/L Tris-HCl buffer (pH 7.5). All reactions were conducted aerobically at 4 °C and were performed in three independent reactions unless otherwise indicated.

To characterize the H_2O_2 dose–response profiles and tolerance of the LPMOs, time-course assays were performed at 4 °C and 0.1 MPa with initial H_2O_2 concentrations ranging from 0 to 1,000 µmol/L. These reactions were performed in 1-mL deep-well plates, with aliquots collected sequentially at 0.25, 1, 2, and 4 h. To examine the effects of H_2O_2 on LPMO-mediated chitin oxidation under pressure, 6 h reactions were performed across the pressure gradient of 0.1–115 MPa with or without exogenous H_2O_2 supplementation. H_2O_2 was added at 50 µmol/L for Meer1P and CBP21 and at 30 µmol/L for Meer2P. These working concentrations were selected on the basis of the dose–response profiles measured at 4 °C and 0.1 MPa, within the range of effective stimulation for each enzyme while limiting exposure to higher H_2O_2 concentrations and potential nonproductive oxidation of ascorbic acid (100 µmol/L) over the longer reaction time[127]. The pressure-gradient assays were designed to compare H_2O_2-supplemented reactions with their corresponding no-added-H_2O_2 controls at each pressure, rather than to compare the magnitude of H_2O_2 stimulation across enzymes. For both the 0.1 MPa and 60–115 MPa treatments, reaction mixtures were loaded into identical sealed syringes and placed in customized pressure-retaining tubes, with the 0.1 MPa reactions maintained without pressurization. For the 60–115 MPa treatments, the target pressure was reached within ~5 min. For all assays, approximately 180 µL aliquots were collected at the designated sampling time(s) and immediately flash-quenched in liquid nitrogen. The quenched samples were then transferred to a 90 °C water bath and heated for 20 min to inactivate the LPMOs, followed by filtration through 0.22 µm filters prior to instrumental analysis.

LC-MS/MS analysis

LC-MS/MS was used for two purposes: analysis and quantification of LPMO-derived oxidized chitooligosaccharides and untargeted metabolomic analysis of the culture samples.

To quantify LPMO-derived oxidized products, ~60 µL of the filtered reaction mixture was incubated overnight at 37 °C with ~1.5 µmol/L SmCHB[62]. This treatment converted

all soluble oxidized products to GlcNAc and DP2ox (GlcNAc–GlcNAc1A). Quantification was based on calibration curves generated with DP2ox standards (0.1–100 µmol/L). DP2ox standards were prepared in-house by complete oxidation of N-acetyl-chitobiose (Anpel, 98% purity) using ChitO[128], as previously described[62].

For untargeted metabolomic analysis of the culture samples, samples were desalted using Copure® PBA solid-phase extraction (SPE) cartridges. Commercial standards of GlcNAc and chitooligosaccharides (DP2–DP6) were analyzed under the same LC-MS/MS conditions, and their retention times and m/z values were used to confirm the corresponding metabolites in the culture samples.

Chromatographic separation was performed on a Waters ACQUITY UPLC® BEH Amide column (2.1 mm × 150 mm) using water with 0.1% formic acid (solvent A) and acetonitrile with 0.1% formic acid (solvent B) at a flow rate of 0.4 mL/min. The gradient was as follows: 5% A from 0 to 1 min, 5%–30% A from 1 to 4 min, 30%–60% A from 4 to 9 min, 60%–100% A from 9 to 9.5 min, 100% A from 9.5 to 10.5 min, 100%–5% A from 10.5 to 11 min, followed by equilibration at 5% A until 12 min. The injection volume was 1 µL, and the column temperature was maintained at 45 °C. MS data were acquired in both positive and negative electrospray ionization modes over an *m/z* range of 50–2,000. The source temperature was 120 °C, desolvation temperature was 400 °C, cone gas flow was 50 L/h, desolvation gas flow was 800 L/h, capillary voltage was 2.0 kV, and sampling cone voltage was 40 V. Low- and high-energy data were acquired with collision energies of 10 eV and 20–40 eV, respectively.

H_2O_2 measurements

The H_2O_2 concentration in LPMO reactions with crystalline α-chitin was measured using a method adapted from a previously reported protocol[38] with some modifications. Before the H_2O_2 depletion assays, stored LPMOs were re-saturated with $CuSO_4$ and immediately desalted to remove free copper. Reaction mixtures contained 2 µmol/L Cu^{2+}-saturated LPMO, 2 mg/mL crystalline α-chitin, 20 µmol/L ascorbic acid (AscA), and 100 µmol/L H_2O_2 in 10 mmol/L Tris-HCl buffer (pH 7.5). Reactions were conducted at 4 °C and 0.1 MPa. Parallel no-LPMO and no-chitin reactions were included as controls. All assays were performed in three independent reactions. To determine H_2O_2 concentration, the supernatant fraction was collected from the reaction mixture and immediately filtered through a 0.22 µm filter to remove any potentially remaining chitin particles. Then, 50 µL of the filtered supernatant was mixed with 50 µL of a premix composed of horseradish peroxidase (HRP; 10 U/mL) and Amplex Red (200 µmol/L, 2% DMSO in the premix) in 10 mmol/L Tris-HCl buffer (pH 7.5). The reaction mixture (100 µL) was incubated in a 96-well microtiter plate for 10 min before recording the absorbance at 563 nm. H_2O_2 was quantified using a standard curve (0–100 µmol/L H_2O_2) prepared in the same buffer containing 20 µmol/L AscA.

The H_2O_2 concentrations in all AP + chitin and HHP + chitin cultures, as well as in the corresponding AP-no-chitin and HHP-no-chitin controls, were measured using a potassium iodide (KI)-based colorimetric assay, in which H_2O_2 oxidizes iodide to generate triiodide (I_3^-)[129]. The H_2O_2 levels were determined spectrophotometrically by monitoring the absorbance of the yellow triiodide complex. We prepared equal volumes of Solution A [containing 400 mmol/L KI (Sigma-Aldrich, Cat#221945), 50 mmol/L NaOH (Sigma-Aldrich, Cat#221465), and 170 µmol/L ammonium molybdate tetrahydrate (Aladdin Scientific, Cat#A116375)] and Solution B [containing 100 mmol/L potassium hydrogen phthalate (Aladdin Scientific, Cat#P434310)], and 50 µL of each solution was mixed. Then, 100 µL of culture supernatant from samples centrifuged at 10,000 × *g* for 10 min was added to the mixture. The reaction was carried out in the dark for 10 min to prevent light-induced alterations. Then the concentration of H_2O_2 was measured using spectrophotometry at the maximum absorption wavelength of 351 nm.

Molecular dynamics (MD) simulations

Structural models of apo- and holo-Meer1P and Meer2P were constructed using AlphaFold3[63], whereas the experimentally determined apo and holo structures of CBP21 were obtained from PDB entries 2BEN[130] and 8RRY[131], respectively. All MD simulations were performed using GROMACS 2025.4[132]. Protein topologies for both the apo and holo forms were generated using the CHARMM36[133] force field. Each holo system contained one Cu^{2+} ion, described by the CHARMM CU2P ion type with its associated Lennard-Jones and electrostatic parameters (charge + 2e; R_min/2 = 1.05 Å; ε = −0.0050 kcal/mol); no explicit Cu–ligand bonded terms were applied. Each system was solvated with the TIP3P water model[134] in a dodecahedral box, neutralized, and supplemented with 0.15 mol/L NaCl. After steepest-descent energy minimization, the systems were equilibrated for 1 ns under the NVT ensemble at 4 °C or 25 °C, followed by 5 ns of NPT equilibration at 0.1 or 80 MPa with position restraints on protein heavy atoms and, for the holo systems, Cu^{2+}. Production simulations were then performed for 100 ns without position restraints, with three replicas for each condition. Simulations used a 2 fs time step with LINCS constraints on bonds involving hydrogen. Electrostatics were treated with PME (real-space cutoff 1.2 nm), and van der Waals interactions with a force-switch from 1.0 to 1.2 nm. Temperature was maintained with the V-rescale thermostat and pressure with the C-rescale barostat at 0.1 MPa or 80 MPa, with an isothermal compressibility of 4.5×10^{-5} bar^{-1}.

DATA AVAILABILITY

The omics datasets, including sequencing and mass spectrometry proteomics data, generated in this study have been deposited in NODE (biosino.org/node) under accession number OEP00007033 and can be accessed by entering the accession number in the search box or directly via the website (biosino.org/node/project/detail/OEP00007033). Additional source data and information required to reanalyze the data reported in this work are available from the corresponding author upon reasonable request.

ACKNOWLEDGEMENTS

This work was financially supported by the Hainan Provincial Natural Science Foundation (426ZD1006), the National Natural Science Foundation of China (42330206, 32530002, and 32570058), Project of State Key Laboratory of Microbial

Metabolism, Shanghai Jiao Tong University (SKLMMZD_02), and Double First-Class Initiative. We thank Dr. Jingli Hou, an associate researcher from the Instrumental Analysis Center of Shanghai Jiao Tong University for her contributions to optimizing enzymatic cleavage methods for proteins and conducting mass spectrometry analysis of peptides. We acknowledge support from the Center for High Performance Computing (HPC) at Shanghai Jiao Tong University for multi-omics analysis in this study. Finally, we extend our profound appreciation to the Institute of Deep-sea Science and Engineering, Chinese Academy of Sciences (IDSSE CAS), for providing critical access to R/V Tan Suo Yi Hao, as well as the HOV *Fendouzhe*. The operational expertise and technical support from the crews and engineers were indispensable to the data acquisition and experimental success of this study.

AUTHOR CONTRIBUTIONS

Conceptualization, W.Z., X.X.; investigation, W.Z., X.X.; methodology, X.Z., W.Z., T.Z., H.Z., A.J., X.X., J.W.; experiments, H.Z., X.Z., T.Z., W.Y., A.J., R.X., S.K.W., W.Z.; software, X.Z., Y.F.L., W.Z., J.W., Z.W., H.Z.; data analysis, X.Z., W.Z., H.Z., T.Z., S.H., Y.Y.L., Y.F.L., Z.W., J.W.; visualization, X.Z., W.Z., H.Z., T.Z., Y.F.L., J.W.; data curation, X.Z., W.Z., J.W.; writing – original draft, X.Z., W.Z.; writing – review & editing, W.Z., X.Z., X.X.; resources, X.X., W.Z.; funding acquisition, X.X., W.Z.; supervision, W.Z., X.X.

COMPETING INTERESTS

The authors declare no competing interests.

REFERENCES

1. Xiao, X., Wang, J. & Ding, K. MEER: Extraordinary flourishing ecosystem in the deepest ocean. *Cell* **188**, 1175–1177 (2025).
2. Xiao, X. et al. Microbial ecosystems and ecological driving forces in the deepest ocean sediments. *Cell* **188**, 1363–1377.e9 (2025).
3. Jamieson, A.J., Fujii, T., Mayor, D.J., Solan, M. & Priede, I.G. Hadal trenches: the ecology of the deepest places on Earth. *Trends. Ecol. Evol.* **25**, 190–197 (2010).
4. Glud, R.N. et al. High rates of microbial carbon turnover in sediments in the deepest oceanic trench on Earth. *Nat. Geosci.* **6**, 284–288 (2013).
5. Wenzhöfer, F. et al. Benthic carbon mineralization in hadal trenches: assessment by *in situ* O_2 microprofile measurements. *Deep Sea Res. Part Oceanogr. Res. Pap.* **116**, 276–286 (2016).
6. Luo, M. et al. Benthic carbon mineralization in hadal trenches: insights from *in situ* determination of benthic oxygen consumption. *Geophys. Res. Lett.* **45**, 2752–2760 (2018).
7. Glud, R.N. et al. Hadal trenches are dynamic hotspots for early diagenesis in the deep sea. *Commun. Earth Environ.* **2**, 21 (2021).
8. Thamdrup, B. et al. Anammox bacteria drive fixed nitrogen loss in hadal trench sediments. *Proc. Natl. Acad. Sci. U. S. A.* **118**, e2104529118 (2021).
9. Yang, N., Lv, Y., Ji, M., Wu, S. & Zhang, Y. High hydrostatic pressure stimulates microbial nitrate reduction in hadal trench sediments under oxic conditions. *Nat. Commun.* **15**, 2473 (2024).
10. Glud, R.N. & Schauberger, C. Element cycling and microbial life in the hadal realm. *Trends. Microbiol.* **32**, 1045–1048 (2024).
11. Picard, A. & Daniel, I. Pressure as an environmental parameter for microbial life—a review. *Biophys. Chem.* **183**, 30–41 (2013).
12. Tamburini, C., Boutrif, M., Garel, M., Colwell, R.R. & Deming, J.W. Prokaryotic responses to hydrostatic pressure in the ocean—a review. *Environ. Microbiol.* **15**, 1262–1274 (2013).
13. Marietou, A. et al. The effect of hydrostatic pressure on enrichments of hydrocarbon degrading microbes from the Gulf of Mexico following the Deepwater Horizon oil spill. *Front. Microbiol.* **9**, 808 (2018).
14. Souza, C.P., Almeida, B.C., Colwell, R.R. & Rivera, I.N. The importance of chitin in the marine environment. *Mar. Biotechnol.* **13**, 823–830 (2011).
15. Moussian, B. Chitin: structure, chemistry and biology. *Adv. Exp. Med. Biol.* **1142**, 5–18 (2019).
16. Capovilla, G. et al. Chitin utilization by marine picocyanobacteria and the evolution of a planktonic lifestyle. *Proc. Natl. Acad. Sci. U. S. A.* **120**, e2213271120 (2023).
17. Keyhani, N.O. & Roseman, S. Physiological aspects of chitin catabolism in marine bacteria. *Biochim. Biophys. Acta.* **1473**, 108–122 (1999).
18. Zhang, H. et al. The amphipod genome reveals population dynamics and adaptations to hadal environment. *Cell* **188**, 1378–1392.e18 (2025).
19. Di Franco, D. et al. Ecological and spatial factors shaping abyssal and hadal peracarid crustacean communities in the eastern Aleutian Trench (NE Pacific). *Prog. Oceanogr.* **241**, 103651 (2025).
20. Ghosh, M., Sadhukhan, S. & Dey, K.K. Elucidating the internal structure and dynamics of α-chitin by 2DPASS-MAS-NMR and spin-lattice relaxation measurements. *Solid. State. Nucl. Magn. Reson.* **97**, 7–16 (2019).
21. Ioelovich, M. Crystallinity and hydrophility of chitin and chitosan. *Res. Rev. J. Chem.* **3**, 7–14 (2014).
22. Goodrich, J.D. & Winter, W.T. Alpha-chitin nanocrystals prepared from shrimp shells and their specific surface area measurement. *Biomacromolecules*. **8**, 252–257 (2007).
23. Lu, Y. et al. Fabrication and characterisation of α-chitin nanofibers and highly transparent chitin films by pulsed ultrasonication. *Carbohydr. Polym.* **98**, 1497–1504 (2013).
24. Mohan, K., Muralisankar, T., Jayakumar, R. & Rajeevgandhi, C. A study on structural comparisons of α-chitin extracted from marine crustacean shell waste. *Carbohydr. Polym. Technol. Appl.* **2**, 100037 (2021).
25. Poshina, D.N., Raik, S.V., Poshin, A.N. & Skorik, Y.A. Accessibility of chitin and chitosan in enzymatic hydrolysis: a review. *Polym. Degrad. Stab.* **156**, 269–278 (2018).
26. Yang, Y. et al. Improving extracellular production of *Serratia marcescens* lytic polysaccharide monooxygenase CBP21 and *Aeromonas veronii* B565 chitinase Chi92 in *Escherichia coli* and their synergism. *AMB Express.* **7**, 170 (2017).
27. Beier, S. & Bertilsson, S. Bacterial chitin degradation-mechanisms and ecophysiological strategies. *Front. Microbiol.* **4**, 149 (2013).
28. Jeuniaux, C. Chitinases. In: Methods in Enzymology. Elsevier, 644–650 (1966).
29. Vaaje-Kolstad, G. et al. An oxidative enzyme boosting the enzymatic conversion of recalcitrant polysaccharides. *Science* **330**, 219–222 (2010).
30. Forsberg, Z. et al. Discovery of a copper-binding carbohydrate-binding module regulating the activity of lytic polysaccharide monooxygenases. *J. Am. Chem. Soc.* **147**, 45104–45118 (2025).
31. Berggreen, H., Emrich-Mills, T.Z., Mathiesen, G., Eijsink, V.G. & Forsberg, Z. Homologous expression and characterization of an LPMO from commensal *Lactiplantibacillus plantarum* WCFS1 and comparison with related enzymes from chitin-degrading bacteria. *ACS Omega.* **11**, 37755–37770 (2026).
32. Middelboe, M., Traving, S.J., Castillo, D., Kalatzis, P.G. & Glud, R.N. Prophage-encoded chitinase gene supports growth of its bacterial host isolated from deep-sea sediments. *ISME J.* **19**, wraf004 (2025).
33. Zhao, X. et al. Diversity of culturable heterotrophic bacteria from the Mariana Trench and their ability to degrade macromolecules. *Mar. Life Sci. Technol.* **2**, 181–193 (2020).
34. Vezzi, A. et al. Life at depth: photobacterium profundum genome sequence and expression analysis. *Science* **307**, 1459–1461 (2005).
35. Balmonte, J.P., Arnosti, C., Bartlett, D.H., Caddell, S. & Glud, R.N. Effects of increasing hydrostatic pressures on marine microbial enzymatic activities. *Limnol. Oceanogr.* **70**, 2632–2644 (2025).
36. Hu, S. et al. High hydrostatic pressure enhances chitinase activity and reveals

metabolic regulation via transcriptomics in an abyssal fungus *Purpureocillium lilacinum* FDZ8Y1. *Microb. Cell Factories* **25**, 5 (2025).
37. Li, Y. et al. Revealing the metabolic potential and environmental adaptation of nematophagous fungus, *Purpureocillium lilacinum*, derived from hadal sediment. *Front. Microbiol.* **15**, 1474180 (2024).
38. Bissaro, B. et al. Oxidative cleavage of polysaccharides by monocopper enzymes depends on H_2O_2. *Nat. Chem. Biol.* **13**, 1123–1128 (2017).
39. Kracher, D. et al. Extracellular electron transfer systems fuel cellulose oxidative degradation. *Science* **352**, 1098–1101 (2016).
40. Bissaro, B., Isaksen, I., Vaaje-Kolstad, G., Eijsink, V.G. & Røhr, Å.K. How a lytic polysaccharide monooxygenase binds crystalline chitin. *Biochemistry.* **57**, 1893–1906 (2018).
41. Friedline, S. et al. Activity-targeted metaproteomics uncovers rare syntrophic bacteria central to anaerobic community metabolism. *Nat. Microbiol.* **10**, 2749–2767 (2025).
42. Wu-Woods, N.J. et al. Microbial-enrichment method enables high-throughput metagenomic characterization from host-rich samples. *Nat. Methods.* **20**, 1672–1682 (2023).
43. Dong, X. et al. Metabolic potential of uncultured bacteria and archaea associated with petroleum seepage in deep-sea sediments. *Nat. Commun.* **10**, 1816 (2019).
44. Pontrelli, S. et al. Metabolic cross-feeding structures the assembly of polysaccharide degrading communities. *Sci. Adv.* **8**, eabk3076 (2022).
45. Zhang, Y. et al. Predicting functions of uncharacterized gene products from microbial communities. *Nat. Biotechnol.* **44**, 1126–1141 (2026).
46. Knop, J.M. et al. Life in multi-extreme environments: brines, osmotic and hydrostatic pressure—a physicochemical view. *Chem. Rev.* **123**, 73–104 (2023).
47. Amano, C. et al. Limited carbon cycling due to high-pressure effects on the deep-sea microbiome. *Nat. Geosci.* **15**, 1041–1047 (2022).
48. Gerringer, M.E. et al. Pressure tolerance of deep-sea enzymes can be evolved through increasing volume changes in protein transitions: a study with lactate dehydrogenases from abyssal and hadal fishes. *FEBS J.* **287**, 5394–5410 (2025).
49. Lloyd, C.C., Balmonte, J.P., Glud, R.N. & Arnosti, C. Strong effects of increased hydrostatic pressure on polysaccharide-hydrolyzing enzyme activities in coastal seawater and sediments. *J. Geophys. Res. Biogeosciences* **130**, e2024JG008417 (2025).
50. Nakagawa, Y.S. et al. A small lytic polysaccharide monooxygenase from *Streptomyces griseus* targeting α- and β-chitin. *FEBS J.* **282**, 1065–1079 (2015).
51. Nakagawa, Y.S., Eijsink, V.G., Totani, K. & Vaaje-Kolstad, G. Conversion of α-chitin substrates with varying particle size and crystallinity reveals substrate preferences of the chitinases and lytic polysaccharide monooxygenase of *Serratia marcescens*. *J. Agric. Food. Chem.* **61**, 11061–11066 (2013).
52. Stewart, H.A. & Jamieson, A.J. Habitat heterogeneity of hadal trenches: considerations and implications for future studies. *Prog. Oceanogr.* **161**, 47–65 (2018).
53. Zhang, X. et al. The hadal zone is an important and heterogeneous sink of black carbon in the ocean. *Commun. Earth Environ.* **3**, 25 (2022).
54. Liu, R. et al. Novel chloroflexi genomes from the deepest ocean reveal metabolic strategies for the adaptation to deep-sea habitats. *Microbiome* **10**, 75 (2022).
55. Seki, H. Microbiological studies on the decomposition of chitin in marine environment-IX rough estimation on chitin decomposition in the ocean. *J. Oceanogr. Soc. Jpn.* **21**, 253–260 (1965).
56. Wishart, D.S. et al. HMDB 5.0: the Human Metabolome Database for (2022). *Nucleic. Acids. Res.* **50**, D622–D631 (2022).
57. Jiang, W.X. et al. A pathway for chitin oxidation in marine bacteria. *Nat. Commun.* **13**, 5899 (2022).
58. Moreno, J., Nielsen, H., Winther, O. & Teufel, F. Predicting the subcellular location of prokaryotic proteins with DeepLocPro. *Bioinformatics* **40**, btae677 (2024).
59. Kato, C. et al. Extremely barophilic bacteria isolated from the Mariana Trench, Challenger Deep, at a depth of 11,000 meters. *Appl. Environ. Microbiol.* **64**, 1510–1513 (1998).
60. Nogi, Y. & Kato, C. Taxonomic studies of extremely barophilic bacteria isolated from the Mariana Trench and description of *Moritella yayanosii* sp. nov., a new barophilic bacterial isolate. *Extremophiles* **3**, 71–77 (1999).
61. Igarashi, K. et al. Traffic jams reduce hydrolytic efficiency of cellulase on cellulose surface. *Science* **333**, 1279–1282 (2011).
62. Loose, J.S., Forsberg, Z., Fraaije, M.W., Eijsink, V.G. & Vaaje-Kolstad, G. A rapid quantitative activity assay shows that the *Vibrio cholerae* colonization factor GbpA is an active lytic polysaccharide monooxygenase. *FEBS Lett.* **588**, 3435–3440 (2014).
63. Abramson, J. et al. Accurate structure prediction of biomolecular interactions with AlphaFold 3. *Nature* **630**, 493–500 (2024).
64. Zhou, Y. et al. Functional characterization of multidomain LPMOs from marine *Vibrio* species reveals modulation of enzyme activity by domain-domain interactions. *Biochemistry* **65**, 90–103 (2026).
65. Huang, Q., Rodgers, J.M., Hemley, R.J. & Ichiye, T. Extreme biophysics: enzymes under pressure. *J. Comput. Chem.* **38**, 1174–1182 (2017).
66. Xiao, X., Zhang, Y. & Wang, F. Hydrostatic pressure is the universal key driver of microbial evolution in the deep ocean and beyond. *Environ. Microbiol. Rep.* **13**, 68–72 (2021).
67. Wang, H., Zhang, Y., Bartlett, D.H. & Xiao, X. Transcriptomic analysis reveals common adaptation mechanisms under different stresses for moderately piezophilic bacteria. *Microb. Ecol.* **81**, 617–629 (2021).
68. Hunt, D.E., Gevers, D., Vahora, N.M. & Polz, M.F. Conservation of the chitin utilization pathway in the *Vibrionaceae*. *Appl. Environ. Microbiol.* **74**, 44–51 (2008).
69. Jung, B.O., Roseman, S. & Park, J.K. The central concept for chitin catabolic cascade in marine bacterium, *Vibrios*. *Macromol. Res.* **16**, 1–5 (2008).
70. Ravin, N.V. et al. Genome analysis of *Fimbriiglobus ruber* $SP5^T$, a planctomycete with confirmed chitinolytic capability. *Appl. Environ. Microbiol.* **84**, e02645–17 (2018).
71. Nunoura, T. et al. Microbial diversity in sediments from the bottom of the Challenger Deep, the Mariana Trench. *Microbes. Environ.* **33**, 186–194 (2018).
72. Zhou, Y.L., Mara, P., Cui, G.J., Edgcomb, V.P. & Wang, Y. Microbiomes in the Challenger Deep slope and bottom-axis sediments. *Nat. Commun.* **13**, 1515 (2022).
73. Nunoura, T. et al. Molecular biological and isotopic biogeochemical prognoses of the nitrification-driven dynamic microbial nitrogen cycle in hadopelagic sediments. *Environ. Microbiol.* **15**, 3087–3107 (2013).
74. Yuan, J. & Shiller, A.M. Hydrogen peroxide in deep waters of the North Pacific Ocean. *Geophys. Res. Lett.* **31**, L01310 (2004).
75. Zhang, W.J. et al. Unveiling active microbial processes in Earth's deepest seawater. *Cell Host Microbe* **34**, 1540–1559.e10 (2026).
76. Liu, Y. et al. Comparison of prokaryotes between Mount Everest and the Mariana Trench. *Microbiome* **10**, 215 (2022).
77. Liu, X. et al. Real-time mapping of a hydrogen peroxide concentration profile across a polymicrobial bacterial biofilm using scanning electrochemical microscopy. *Proc. Natl. Acad. Sci. U. S. A.* **108**, 2668–2673 (2011).
78. Hoang, N.H., Golten, O., Forsberg, Z., Eijsink, V.G. & Richter, M. *In situ* H_2O_2 generation by choline oxidase and its application in amino polysaccharide degradation by coupling to lytic polysaccharide monooxygenase. *ChemBioChem* **24**, e202300363 (2023).
79. Kommedal, E.G. et al. Visible light-exposed lignin facilitates cellulose solubilization by lytic polysaccharide monooxygenases. *Nat. Commun.* **14**, 1063 (2023).
80. Gao, W., Li, T., Zhou, H., Ju, J. & Yin, H. Carbohydrate-binding modules enhance H_2O_2 tolerance by promoting lytic polysaccharide monooxygenase active site H_2O_2 consumption. *J. Biol. Chem.* **300**, 105573 (2024).
81. Zhao, W. & Xiao, X. Seeking the invisible microbial oases in extreme environments. *Cell Host Microbe* **34**, 1504–1508 (2026).

82. Xu, M. et al. Multimodal AI decodes extreme environment functional dark matter beyond homology. Preprint at *bioRxiv*, 2025.11.15.688615 (2025).
83. Rothschild, L.J. & Mancinelli, R.L. Life in extreme environments. *Nature* **409**, 1092–1101 (2001).
84. Zhong, M., Li, Y., Deng, L., Fang, J. & Yu, X. Insight into the adaptation mechanisms of high hydrostatic pressure in physiology and metabolism of hadal fungi from the deepest ocean sediment. *Msystems* **9**, e01085–23 (2024).
85. Cario, A., Jebbar, M., Thiel, A., Kervarec, N. & Oger, P.M. Molecular chaperone accumulation as a function of stress evidences adaptation to high hydrostatic pressure in the piezophilic archaeon *Thermococcus barophilus*. *Sci. Rep.* **6**, 29483 (2016).
86. Yayanos, A.A., Dietz, A.S. & Boxtel, R.V. Isolation of a deep-sea barophilic bacterium and some of its growth characteristics. *Science* **205**, 808–810 (1979).
87. Moalic, Y. et al. Regulation of gene expression under high hydrostatic pressure: the versatile role of the master regulator SurR in energy metabolism. *Front. Microbiol.* **16**, 1593936 (2025).
88. Imai, K., Noda, Y., Adachi, H. & Yoda, K. A novel endoplasmic reticulum membrane protein Rcr1 regulates chitin deposition in the cell wall of *Saccharomyces cerevisiae*. *J. Biol. Chem.* **280**, 8275–8284 (2005).
89. Schneider, C.A., Rasband, W.S. & Eliceiri, K.W. NIH image to ImageJ: 25 years of image analysis. *Nat. Methods.* **9**, 671–675 (2012).
90. Horn, S.J. & Eijsink, V.G. A reliable reducing end assay for chito-oligosaccharides. *Carbohydr. Polym.* **56**, 35–39 (2004).
91. Albert, D.B. & Martens, C.S. Determination of low-molecular-weight organic acid concentrations in seawater and pore-water samples via HPLC. *Mar. Chem.* **56**, 27–37 (1997).
92. Patton, C.J. & Crouch, S.R. Spectrophotometric and kinetics investigation of the Berthelot reaction for the determination of ammonia. *Anal. Chem.* **49**, 464–469 (1977).
93. Chen, S., Zhou, Y., Chen, Y. & Gu, J. fastp: an ultra-fast all-in-one FASTQ preprocessor. *Bioinformatics* **34**, i884–i890 (2018).
94. Li, D., Liu, C.M., Luo, R., Sadakane, K. & Lam, T.W. MEGAHIT: an ultra-fast single-node solution for large and complex metagenomics assembly via succinct *de Bruijn* graph. *Bioinformatics* **31**, 1674–1676 (2015).
95. Bushnell, B. BBMap: a fast, accurate, splice-aware aligner. (2014)
96. Kang, D.D. et al. MetaBAT 2: an adaptive binning algorithm for robust and efficient genome reconstruction from metagenome assemblies. *PeerJ.* **7**, e7359 (2019).
97. Wu, Y.W., Simmons, B.A. & Singer, S.W. MaxBin 2.0: an automated binning algorithm to recover genomes from multiple metagenomic datasets. *Bioinformatics* **32**, 605–607 (2016).
98. Alneberg, J. et al. Binning metagenomic contigs by coverage and composition. *Nat. Methods.* **11**, 1144–1146 (2014).
99. Nissen, J.N. et al. Improved metagenome binning and assembly using deep variational autoencoders. *Nat. Biotechnol.* **39**, 555–560 (2021).
100. Liu, C.C. et al. MetaDecoder: a novel method for clustering metagenomic contigs. *Microbiome* **10**, 46 (2022).
101. Orakov, A. et al. GUNC: detection of chimerism and contamination in prokaryotic genomes. *Genome. Biol.* **22**, 178 (2021).
102. Olm, M.R., Brown, C.T., Brooks, B. & Banfield, J.F. dRep: a tool for fast and accurate genomic comparisons that enables improved genome recovery from metagenomes through de-replication. *ISME J.* **11**, 2864–2868 (2017).
103. Li, H. Aligning sequence reads, clone sequences and assembly contigs with BWA-MEM. Preprint at *arXiv*, 1303.3997 (2013)
104. Aroney, S.T.N. et al. CoverM: read alignment statistics for metagenomics. *Bioinformatics* **41**, btaf147 (2025).
105. Camargo, A.P. et al. Identification of mobile genetic elements with geNomad. *Nat. Biotechnol.* **42**, 1303–1312 (2024).
106. Hyatt, D. et al. Prodigal: prokaryotic gene recognition and translation initiation site identification. *BMC. Bioinformatics* **11**, 119 (2010).
107. Queirós, P., Delogu, F., Hickl, O., May, P. & Wilmes, P. Mantis: flexible and consensus-driven genome annotation. *GigaScience* **10**, giab042 (2021).
108. Menzel, P., Ng, K.L. & Krogh, A. Fast and sensitive taxonomic classification for metagenomics with kaiju. *Nat. Commun.* **7**, 11257 (2016).
109. Patro, R., Duggal, G., Love, M.I., Irizarry, R.A. & Kingsford, C. Salmon provides fast and bias-aware quantification of transcript expression. *Nat. Methods.* **14**, 417–419 (2017).
110. Yu., F. et al. Fast quantitative analysis of timsTOF PASEF Data with MSFragger and IonQuant. *Mol. Cell Proteomics.* **19**, 1575–1585 (2020).
111. Kong, A.T., Leprevost, F.V., Avtonomov, D.M., Mellacheruvu, D. & Nesvizhskii, A.I. MSFragger: ultrafast and comprehensive peptide identification in mass spectrometry-based proteomics. *Nat. Methods.* **14**, 513–520 (2017).
112. da Veiga Leprevost, F. et al. Philosopher: a versatile toolkit for shotgun proteomics data analysis. *Nat. Methods.* **17**, 869–870 (2020).
113. Yang, K.L. et al. MSBooster: improving peptide identification rates using deep learning-based features. *Nat. Commun.* **14**, 4539 (2023).
114. The, M., MacCoss, M.J., Noble, W.S. & Käll, L. Fast and accurate protein false discovery rates on large-scale proteomics data sets with percolator 3.0. *J. Am. Soc. Mass. Spectrom.* **27**, 1719–1727 (2016).
115. Nesvizhskii, A.I., Keller, A., Kolker, E. & Aebersold, R. A statistical model for identifying proteins by tandem mass spectrometry. *Anal. Chem.* **75**, 4646–4658 (2003).
116. Yu, F., Haynes, S.E. & Nesvizhskii, A.I. IonQuant enables accurate and sensitive label-free quantification with FDR-Controlled Match-Between-Runs. *Mol. Cell Proteomics.* **20**, 100077 (2021).
117. Meunier, L. et al. Selection of marine bacterial consortia efficient at degrading chitin leads to the discovery of new potential chitin degraders. *Microbiol. Spectr.* **12**, e0088624 (2024).
118. Turner, S., Pryer, K.M., Miao, V.P. & Palmer, J.D. Investigating deep phylogenetic relationships among cyanobacteria and plastids by small subunit rRNA sequence analysis. *J. Eukaryot. Microbiol.* **46**, 327–338 (1999).
119. Apprill, A., McNally, S., Parsons, R. & Weber, L. Minor revision to V4 region SSU rRNA 806R gene primer greatly increases detection of SAR11 bacterioplankton. *Aquat. Microb. Ecol.* **75**, 129–137 (2015).
120. Yang, S. et al. Genomic and enzymatic evidence of acetogenesis by anaerobic methanotrophic archaea. *Nat. Commun.* **11**, 3941 (2020).
121. Fu, L., Niu, B., Zhu, Z., Wu, S. & Li, W. CD-HIT: accelerated for clustering the next-generation sequencing data. *Bioinformatics* **28**, 3150–3152 (2012).
122. Katoh, K. & Standley, D.M. MAFFT multiple sequence alignment software version 7: improvements in performance and usability. *Mol. Biol. Evol.* **30**, 772–780 (2013).
123. Capella-Gutiérrez, S., Silla-Martínez, J.M. & Gabaldón, T. trimAl: a tool for automated alignment trimming in large-scale phylogenetic analyses. *Bioinformatics* **25**, 1972–1973 (2009).
124. Minh, B.Q. et al. IQ-TREE 2: new models and efficient methods for phylogenetic inference in the genomic era. *Mol. Biol. Evol.* **37**, 1530–1534 (2020).
125. Paoli, L. et al. Biosynthetic potential of the global ocean microbiome. *Nature* **607**, 111–118 (2022).
126. Buchfink, B., Xie, C. & Huson, D.H. Fast and sensitive protein alignment using DIAMOND. *Nat. Methods.* **12**, 59–60 (2015).
127. Müller, G., Chylenski, P., Bissaro, B., Eijsink, V.G. & Horn, S.J. The impact of hydrogen peroxide supply on LPMO activity and overall saccharification efficiency of a commercial cellulase cocktail. *Biotechnol. Biofuels* **11**, 209 (2018).
128. Heuts, D.P., Winter, R.T., Damsma, G.E., Janssen, D.B. & Fraaije, M.W. The role of double covalent flavin binding in chito-oligosaccharide oxidase from Fusarium graminearum. *Biochem. J.* **413**, 175–183 (2008).
129. Klassen, N.V., Marchington, D. & McGowan, H.C. H_2O_2 determination by the I_3^- and by $KMnO_4$ titration. *Anal. Chem.* **66**, 2921–2925 (1994).
130. Vaaje-Kolstad, G., Houston, D.R., Riemen, A.H., Eijsink, V.G. & van Aalten, D.M. Crystal structure and binding properties of the *Serratia marcescens* chitin-binding protein CBP21. *J. Biol. Chem.* **280**, 11313–11319 (2005).
131. Munzone, A. et al. Integrated experimental and theoretical investigation of

copper active site properties of a lytic polysaccharide monooxygenase from *Serratia marcescens*. *Inorg. Chem.* **63**, 11063–11078 (2024).

132. Abraham, M.J. et al. GROMACS: High performance molecular simulations through multi-level parallelism from laptops to supercomputers. *SoftwareX* **1**, 19–25 (2015).
133. Best, R.B. et al. Optimization of the additive CHARMM all-atom protein force field targeting improved sampling of the backbone φ, ψ and side-chain χ_1 and χ_2 dihedral angles. *J. Chem. Theory. Comput.* **8**, 3257–3273 (2012).
134. Jorgensen, W.L., Chandrasekhar, J., Madura, J.D., Impey, R.W. & Klein, M.L. Comparison of simple potential functions for simulating liquid water. *J. Chem. Phys.* **79**, 926–935 (1983).

ADDITIONAL INFORMATION

Supplementary information The online version contains supplementary material available at https://doi.org/10.2738/vita.microbiology.2026.10.0002.

Correspondence and requests for materials should be addressed to Xiang Xiao and Weishu Zhao.

Reprints and permission information is available at https://www.vita-journal.com/microbiology.

© The Author(s) 2026. Published by Higher Education Press. This is an Open Access article distributed under the terms of the CC BY license (https://creativecommons.org/licenses/by/4.0/).